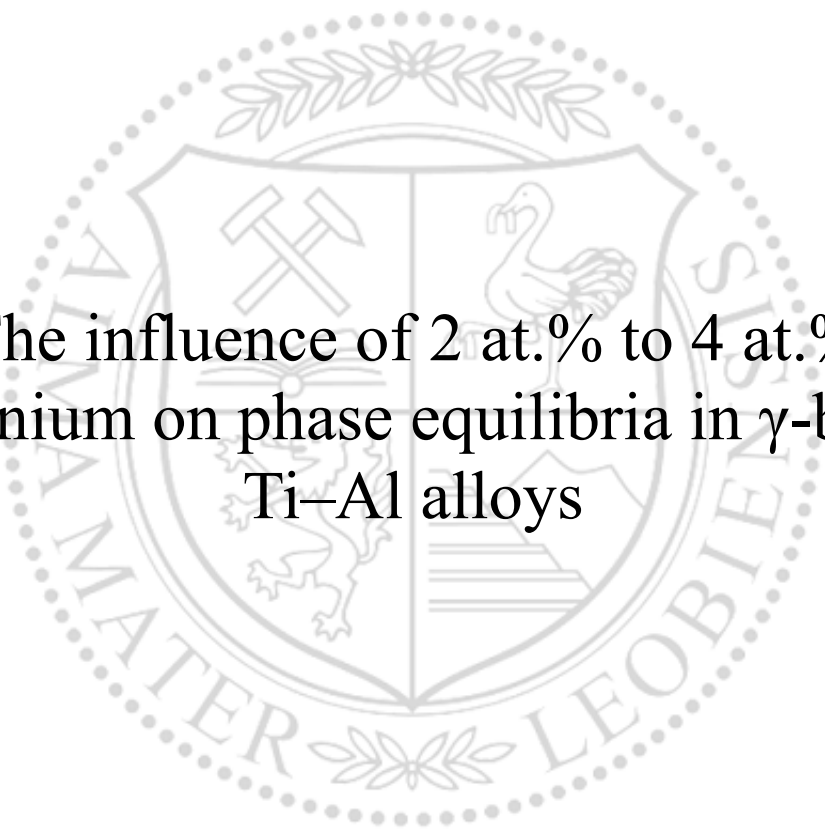




Chair of Physical Metallurgy and Metallic Materials

Master's Thesis



The influence of 2 at.% to 4 at.%  
zirconium on phase equilibria in  $\gamma$ -based  
Ti–Al alloys

Stefan Kardos, BSc

March 2021



**MONTANUNIVERSITÄT LEOBEN**  
www.unileoben.ac.at

**AFFIDAVIT**

I declare on oath that I wrote this thesis independently, did not use other than the specified sources and aids, and did not otherwise use any unauthorized aids.

I declare that I have read, understood, and complied with the guidelines of the senate of the Montanuniversität Leoben for "Good Scientific Practice".

Furthermore, I declare that the electronic and printed version of the submitted thesis are identical, both, formally and with regard to content.

Date 07.03.2021

A handwritten signature in black ink, appearing to read 'Stefan Kardos', written over a horizontal line.

Signature Author  
Stefan Kardos

# Contents

<b>List of Figures</b>	<b>v</b>
<b>List of Tables</b>	<b>vi</b>
<b>List of Abbreviations and Symbols</b>	<b>vii</b>
<b>1 Introduction</b>	<b>1</b>
<b>2 Fundamentals</b>	<b>2</b>
2.1 Binary Ti–Al Phase Diagram . . . . .	2
2.2 Influence of Zr on the Ti–Al System . . . . .	5
2.2.1 Thermodynamics . . . . .	5
2.2.2 Mechanical Properties . . . . .	8
2.2.3 Oxidation Behavior . . . . .	11
<b>3 Experimental</b>	<b>13</b>
3.1 Sample Material . . . . .	13
3.2 Differential Scanning Calorimetry . . . . .	14
3.3 Sample preparation . . . . .	14
3.4 Heat Treatments and Analysis of Microstructure . . . . .	15
3.5 X-ray Diffraction . . . . .	16
3.6 <i>In-situ</i> High-Energy X-ray Diffraction . . . . .	16
3.7 Nanoindentation . . . . .	17
<b>4 Results</b>	<b>20</b>
4.1 Ti–Al–2Zr . . . . .	20
4.1.1 Microstructural Characterization . . . . .	20
4.1.2 DSC Analysis . . . . .	22
4.1.3 High-Energy X-ray Diffraction . . . . .	25
4.2 Ti–Al–4Zr . . . . .	25
4.2.1 DSC Analysis . . . . .	25

4.2.2	Microstructural Characterization . . . . .	26
4.2.3	Conventional and High-Energy X-ray Diffraction . . . . .	28
4.2.4	Nanoindentation . . . . .	30
4.3	Ti–Al–8Zr . . . . .	30
4.4	Phase Diagrams . . . . .	32
4.5	Oxidation Resistance . . . . .	33
<b>5</b>	<b>Discussion</b>	<b>35</b>
5.1	Microstructural Characterization . . . . .	35
5.2	High-Energy X-ray Diffraction . . . . .	36
5.3	Phase Diagrams . . . . .	36
5.4	X-ray Diffraction . . . . .	38
5.5	Nanoindentation . . . . .	38
5.6	Oxidation Resistance . . . . .	39
<b>6</b>	<b>Conclusion</b>	<b>40</b>
	<b>Bibliography</b>	<b>42</b>

# List of Figures

2.1	Binary Ti–Al phase diagram section and $L1_0$ structure of $\gamma$ TiAl . . . . .	3
2.2	Four principal types of microstructures in $\gamma$ TiAl based alloys . . . . .	5
2.3	Binary phase diagrams for the Ti–Zr and Zr–Al systems . . . . .	6
2.4	Partial isothermal sections and liquidus projection of the Ti–Al–Zr system	7
2.5	Temperature dependent compressive stress and strain in Ti–Al–Zr alloys .	10
2.6	Oxidation stages and oxide scale formation in binary Ti–Al alloys . . . . .	12
3.1	Exemplary evaluation of differential scanning calorimetry curves . . . . .	15
3.2	Synchrotron diffraction patterns below and above solidus temperature . . .	18
3.3	Determination of inverse pole figures through electron backscatter diffraction	18
4.1	Polarized light micrographs of heat treated Ti–Al–2Zr samples . . . . .	21
4.2	Microstructure of Ti–46.5Al–2Zr water quenched from 1470 °C . . . . .	22
4.3	Differential scanning calorimetry curves for Ti–Al–2Zr . . . . .	23
4.4	Differential scanning calorimetry curves for Ti–46.5Al–4Zr . . . . .	26
4.5	Polarized light micrographs of heat treated Ti–Al–4Zr samples . . . . .	27
4.6	Microstructure of Ti–46.5Al–4Zr water quenched from 1430 °C . . . . .	28
4.7	Nanoindentation hardness and modulus for the $\gamma$ phase of Ti–46.5Al–4Zr .	31
4.8	Directional hardness and Young’s modulus of $\gamma$ TiAl in Ti–46.5Al–4Zr . . .	31
4.9	Isoplethal sections for Ti–Al–2Zr, Ti–Al–4Zr and Ti–46.5Al–Zr . . . . .	32
4.10	Macroscopic image of oxidation in samples with different Zr contents . . .	34

# List of Tables

2.1	Crystallographic data and temperature stability ranges of relevant phases . . . . .	3
2.2	Hardness and modulus of $\gamma$ TiAl measured via nanoindentation . . . . .	11
3.1	Compositions of the ingot alloy material used in this work . . . . .	13
4.1	Phase transition temperatures of Ti–Al–2Zr alloys . . . . .	24
4.2	Synchrotron phase transition temperatures for Ti–46.5Al–2.1Zr . . . . .	25
4.3	Phase transition temperatures of Ti–46.5Al–4Zr . . . . .	26
4.4	Phase fractions of heat treated Ti–Al–4Zr samples . . . . .	29
4.5	Synchrotron phase transition temperatures for 4 at.% and 8 at.% Zr alloys . . . . .	30
4.6	Oxidation mass increase for samples with different Zr contents . . . . .	34
5.1	Comparison of mechanical properties found during nanoindentation . . . . .	39

# List of Abbreviations and Symbols

at.%	Atomic percent
BSE	Backscattered electrons
CALPHAD	Calculation of phase diagrams
CGHE	Carrier gas hot extraction
CSM	Continuous stiffness measurement
DSC	Differential scanning calorimetry
EBSD	Electron backscatter diffraction
EDX	Energy-dispersive X-ray spectroscopy
F	Face-centered lattice type in Pearson symbols and space group notation
FIB	Focused ion beam
HIP	Hot isostatic pressing
HT	Heat treatment
I	Body-centered lattice type in Pearson symbols and space group notation
ICP-OES	Inductively coupled plasma optical emission spectroscopy
IPF	Inverse pole figure
IQ	Image quality
P	Primitive lattice type in Pearson symbols and space group notation
SEM	Scanning electron microscopy/microscope
SPS	Spark plasma sintering
XRD	X-ray diffraction
XRF	X-ray fluorescence
$\alpha$	Low-temperature allotrope of Ti, A3 crystal structure (unordered)
$\alpha_2$	Ordered, intermetallic Ti <sub>3</sub> Al with D0 <sub>19</sub> crystal structure
$\beta$	High-temperature allotrope of Ti, A2 crystal structure (unordered)
$\beta_o$	Ordered variation of solid solution $\beta$ Ti with B2 crystal structure
$\gamma$	Ordered intermetallic TiAl with L1 <sub>0</sub> crystal structure
$\gamma_m$	Intermetallic $\gamma$ TiAl formed from $\alpha$ Ti via massive transformation

# Chapter 1

## Introduction

Intermetallic  $\gamma$  TiAl based alloys see their use in high temperature applications where materials low in density are required. In search of balanced mechanical properties at room temperature as well as at service temperature, research efforts are directed toward alloying elements which increase the strength of the  $\gamma$  phase over a broad temperature range [1].

One of these elements is thought to be Zr [2], [3]. This work investigates its effect on mechanical and thermodynamic properties of the Ti–Al system between Al contents of 42.5 at.% and 49.5 at.%. Appel *et al.* [4] occasionally gave this range, typical for engineering alloys based on the  $\gamma$  phase, as a starting point for the development of ternary alloys. The contents of Zr in this work's alloys range from 0 at.% to 8 at.%. Higher concentrations of Zr go beyond its solubility in the  $\gamma$  phase, reported by Yang *et al.* [5] to be 9 at.% at 1000 °C and 11 at.% by Kainuma *et al.* [6] at both 1200 °C and 1300 °C.

With respect to the thermodynamic influences of Zr on the Ti–Al system, the aim of this work was the determination of phase transition temperatures above 1000 °C in the aforementioned compositional ranges. To this end, polarized light microscopy and X-ray diffraction (XRD) were used to get an insight into the microstructure of heat-treated and water quenched samples at selected temperatures. Differential scanning calorimetry (DSC) and synchrotron high-energy X-ray diffraction were employed to gain *in-situ* information on phase transitions while samples were heated up to solidus temperature. To characterize the mechanical properties of the  $\gamma$  phase subject to added Zr, nanoindentation was done on a Ti–46.5Al–4Zr alloy. Electron backscatter diffraction (EBSD) was used to correlate the orientation of the indented  $\gamma$  grains to their mechanical properties.

Among the results of this work are partial isopleths for the alloys containing 2 at.% and 4 at.% Zr as well as the directional hardness and Young's modulus for Ti–46.5Al–4Zr. To put these results into perspective, a review of current literature relevant to this work is presented in Chapter 2 and compared to this work's findings in Chapter 5.



# Chapter 2

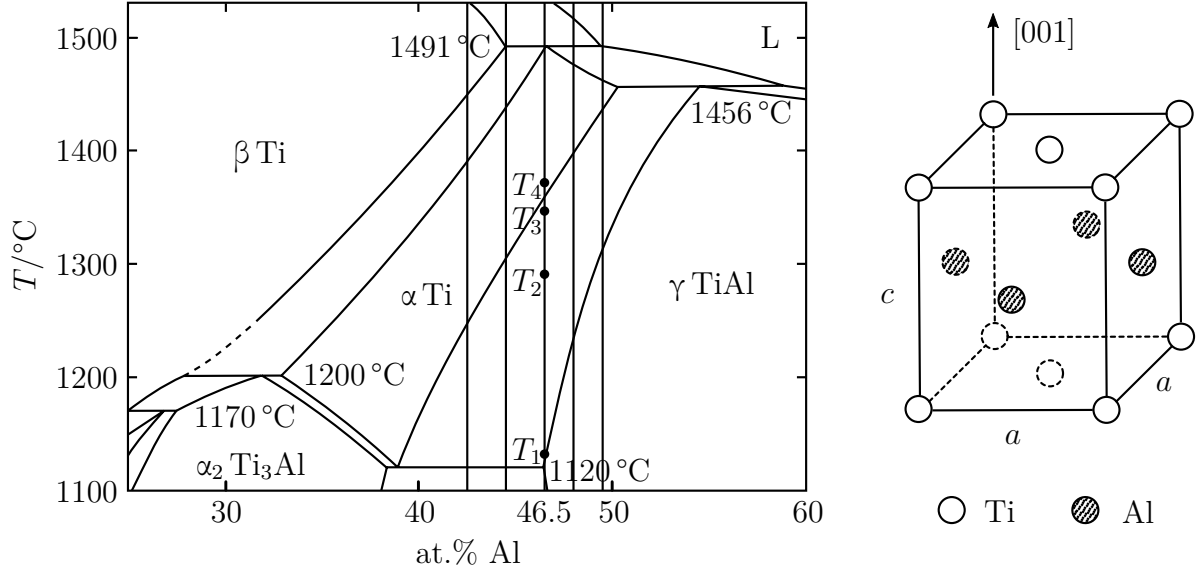
## Fundamentals

### 2.1 Binary Ti–Al Phase Diagram

Several publications investigated the binary Ti–Al system about a decade ago [7], [8]. The one by Schuster and Palm [9] remains authoritative, it thoroughly relies on experimental findings. Shown in Figure 2.1(a) is a section of the binary phase diagram taken from their work. Ranging from 25 at.% to 60 at.% Al, it displays an area of particular interest for the development and application of engineering alloys based on  $\alpha_2$  Ti<sub>3</sub>Al and  $\gamma$  TiAl [4]. The nominal Al contents of the ternary alloys investigated in this work (between 42.5 at.% and 49.5 at.%) are marked by vertical bars. For a detailed overview of the sample material used in this work, see Table 3.1. For the full Ti–Al phase diagram, refer to [9].

According to Appel *et al.* [4], engineering Ti–Al alloys based on the  $\gamma$  phase generally contain between 44 at.% and 48 at.% Al. At room temperature as well as at the intended service temperature of about 700 °C, these alloys always contain both the ordered  $\gamma$  and  $\alpha_2$  phases. They can solidify either peritectically or via the  $\beta$  single-phase field. The solid transformations in equilibrium are  $\beta \rightarrow \alpha + \beta \rightarrow \alpha$ , where two single-phase fields are involved, and  $\alpha \rightarrow \alpha + \gamma \rightarrow \alpha_2 + \gamma$ . At differing cooling rates, other solid phase transformations like the massive  $\alpha \rightarrow \gamma_m$  reaction or the precipitation of  $\gamma$  lamellae from  $\alpha$  can be observed as well. This number of solid transformations allows for sophisticated heat treatment and microstructure development of binary Ti–Al alloys. Table 2.1 gives an overview of crystallographic data and temperature stability regions for the most important phases of this work.

The type of microstructure achieved by heat treating  $\gamma$  TiAl based alloys depends mainly on the volume phase fractions at annealing temperature. Kim [10] described four main classes of microstructures in an alloy consisting of  $\alpha_2$  Ti<sub>3</sub>Al and  $\gamma$  TiAl: near- $\gamma$ , duplex, nearly lamellar and fully lamellar. Near- $\gamma$  microstructure consists mainly of globular and fine  $\gamma$  grains. It is found in samples annealed at temperatures where  $\gamma$  TiAl is the majority



(a) Section of the Ti–Al phase diagram

(b) L<sub>10</sub> structure of  $\gamma$  TiAl

**Figure 2.1:** (a) High-temperature section of the binary Ti–Al phase diagram from 25 at.% to 60 at.% Al as suggested by [9], modified. The position of the  $\beta$  transus line could not be determined with certainty, indicated by a dashed line. Vertical lines mark the nominal Al contents (the pseudo-binary compositions) of the alloys investigated in this work, see Table 3.1.  $T_1$  to  $T_4$  are exemplary heat treatment temperatures to achieve respectively near- $\gamma$ , duplex, nearly lamellar and fully lamellar microstructure in Ti–46.5Al, following a description by [10]. (b) Tetragonal L<sub>10</sub> structure of  $\gamma$  TiAl according to [11], modified.

**Table 2.1:** Important phases for this work together with crystallographic data and temperature stability ranges according to [12]. The first letters of the Pearson symbols denote the crystal systems cubic, hexagonal and tetragonal. The capital letters P, F and I indicate the primitive, face-centered and body-centered lattice types. Zr<sub>5</sub>Al<sub>3</sub> was included because it is part of the isothermal sections of the Ti–Al–Zr system in Section 2.2.1.

Phase	Strukturbericht	Pearson Symbol	Space Group	Stability Range/°C
Al	A1	$cF4$	$Fm\bar{3}m$	up to 665.6
$\alpha$ Ti	A3	$hP2$	$P6_3/mmc$	up to 842
$\beta$ Ti	A2	$cI2$	$Im\bar{3}m$	842 to 1668
$\beta_o$ Ti	B2	$cP2$	$Pm\bar{3}m$	—
$\gamma$ TiAl	L1 <sub>0</sub>	$tP4$	$P4/mmm$	up to 1456
$\alpha_2$ Ti <sub>3</sub> Al	D0 <sub>19</sub>	$hP8$	$P6_3/mmc$	up to 1193
$\alpha$ Zr	A3	$hP2$	$P6_3/mmc$	up to 866
$\beta$ Zr	A2	$cI2$	$Im\bar{3}m$	866 to 1855
Zr <sub>5</sub> Al <sub>3</sub>	D8 <sub>m</sub>	$tI32$	$I4/mcm$	1014 to 1381

phase, close to the eutectoid temperature, see for example  $T_1$  in Figure 2.1(a). In duplex microstructure, the growth of  $\alpha$  grains is inhibited by presence of the  $\gamma$  phase, resulting in a very fine microstructure. This is achieved by heat treating at temperatures where the volume fractions of  $\alpha$  Ti and  $\gamma$  TiAl are about the same ( $T_2$  in Figure 2.1(a)). At higher temperatures,  $\alpha$  becomes the majority phase during heat treatment, leading to larger  $\alpha$  than  $\gamma$  grains. Depending on the volume fraction of the  $\alpha$  grains, a nearly lamellar or a fully lamellar microstructure can be realized. The fully lamellar variant occurs in samples annealed above the  $\alpha$  transus temperature, where rapid growth of  $\alpha$  grains takes place ( $T_4$  in Figure 2.1(a)). During cooling, thin  $\gamma$  lamellae precipitate and form lamellar structures. The following ordering of the  $\alpha$  phase  $\alpha + \gamma \rightarrow \alpha_2 + \gamma$  yields a fully lamellar microstructure, consisting only of  $\alpha_2/\gamma$  colonies. The  $\gamma$  lamellae follow the Blackburn orientation relationship

$$(0001)_{\alpha_2} \parallel \{111\}_{\gamma} \text{ and } \langle 11\bar{2}0 \rangle_{\alpha_2} \parallel \langle 1\bar{1}0 \rangle_{\gamma}, \quad (2.1)$$

where mixed angle and square brackets  $\langle uvw \rangle$  denote a fixed last index, while allowing all possible permutations of the first two indices. The hexagonal phases  $\alpha$  and  $\alpha_2$  share one basal plane, thus the orientation relationship leads to  $\alpha_2$  and  $\gamma$  lamellae that are parallel over all of a former  $\alpha$  grain [4].

Annealing close to but not above the  $\alpha$  transus temperature (see  $T_3$  in Figure 2.1(a)), not the whole microstructure is transformed to  $\alpha$  Ti and a small fraction of  $\gamma$  grains remains in the sample. During near-equilibrium cooling,  $\gamma$  lamellae precipitate from the  $\alpha$  grains just as before, leading to a nearly lamellar microstructure [10]. Figure 2.2 shows these four principal types of microstructures [13].

Since deformation in engineering Ti–Al alloys is for the most part restricted to the  $\gamma$  phase [4], it deserves special interest. Figure 2.1(b) shows its  $L1_0$  crystal structure according to [11], Ti and Al atoms are alternately stacked on the (001) and (002) planes. Lattice parameters vary with temperature and especially Al content [9]. The  $c/a$  ratio at 50 at.% Al is slightly larger than one, yielding a tetragonal unit cell. In Section 2.2.2, the implications of this tetragonality on the mechanical properties of  $\gamma$  TiAl are discussed with respect to the addition of Zr.

Similar to  $\alpha$  Ti with its ordered variant  $\alpha_2$  Ti<sub>3</sub>Al, the  $\beta$  phase can also undergo ordering to  $\beta_o$ . When constructing their binary Ti–Al phase diagram, Schuster and Palm [9] did not incorporate this B2-type ordering of  $\beta$  Ti. Instead, they designated  $\beta$  transus between 1200 °C and 1250 °C with a dashed line, stating the necessity of investigating ternary alloys to be able to determine its position with certainty. Palm, one of the authors of [9], was involved in a recent work on the ternary system Ti–Al–Zr [14] where the current knowledge on B2-type ordering of the  $\beta$  phase was reassessed. The authors came to the conclusion

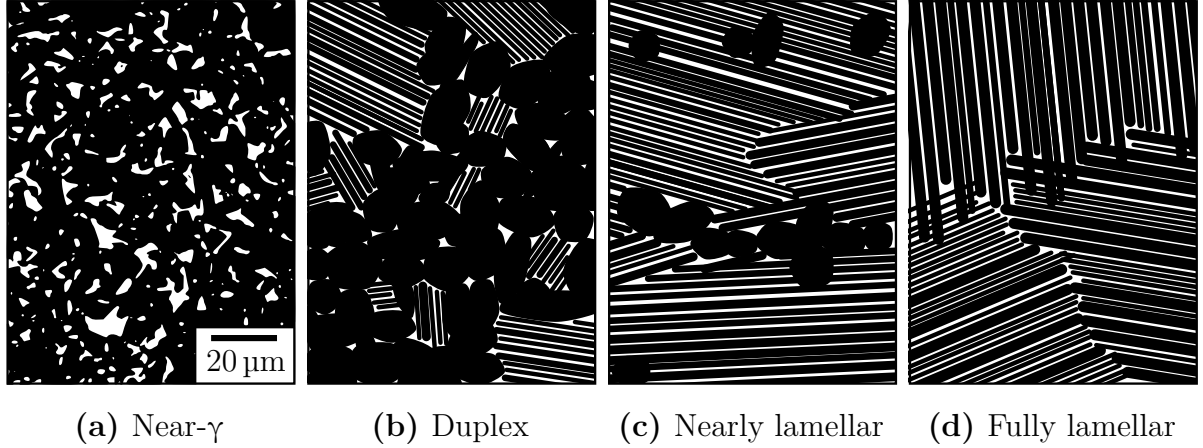


**Figure 2.2:** (a)–(d) Four principal types of microstructures in  $\gamma$  TiAl based alloys according to [13], modified. They can be realized by heat treatment at the temperatures  $T_1$  to  $T_4$  in Figure 2.1(a).  $\gamma$  TiAl is shown as a dark phase, while  $\alpha_2$  Ti<sub>3</sub>Al is shown in white. This is also the way they appear in back scatter electron (BSE) mode during scanning electron microscopy (SEM).

that the ordered  $\beta_o$  phase only appears in binary Ti–Al when taking into account vacancies and antisite defects, which is why it cannot be observed in models of defect-free Ti–Al. In experiment, B2-type ordering stabilizes  $\beta$  Ti up to higher Al contents, as described in [9]. This means that the dashed line in Figure 2.1(a) is actually located further to the right. To stabilize  $\beta$  phase down to room temperature, the alloying of ternary elements is needed.

## 2.2 Influence of Zr on the Ti–Al System

### 2.2.1 Thermodynamics

Like Ti, Zr is in group 4 of the periodic table, so the two elements are chemically similar. At 1855 °C, Zr has a higher melting point than Ti with 1668 °C. At high temperatures, they are totally miscible and form the solid solutions  $\alpha$  and  $\beta$ , spanning the whole composition range. The binary Ti–Zr phase diagram by Turchanin *et al.* [15] demonstrates this, see Figure 2.3(a). A minimum in the system’s solidus and liquidus temperature is located at 35 at.% Zr and 1537 °C. The density of Zr, 6.5 g cm<sup>-3</sup>, is higher than that of Ti, 4.5 g cm<sup>-3</sup> [1]. Thus, alloying Zr to Ti–Al while keeping the Al content constant will make the alloy heavier.

The full phase diagram for the Zr–Al system was recently evaluated by Fischer and Colinet [16], it is shown in Figure 2.3(b). Beside the solid solutions Al,  $\alpha$  Zr and  $\beta$  Zr, ten compounds with narrow homogeneity ranges are present. Zr<sub>5</sub>Al<sub>3</sub> is the only one of them present in the partial isothermal sections of the Ti–Al–Zr system in Figure 2.4. Yang *et*

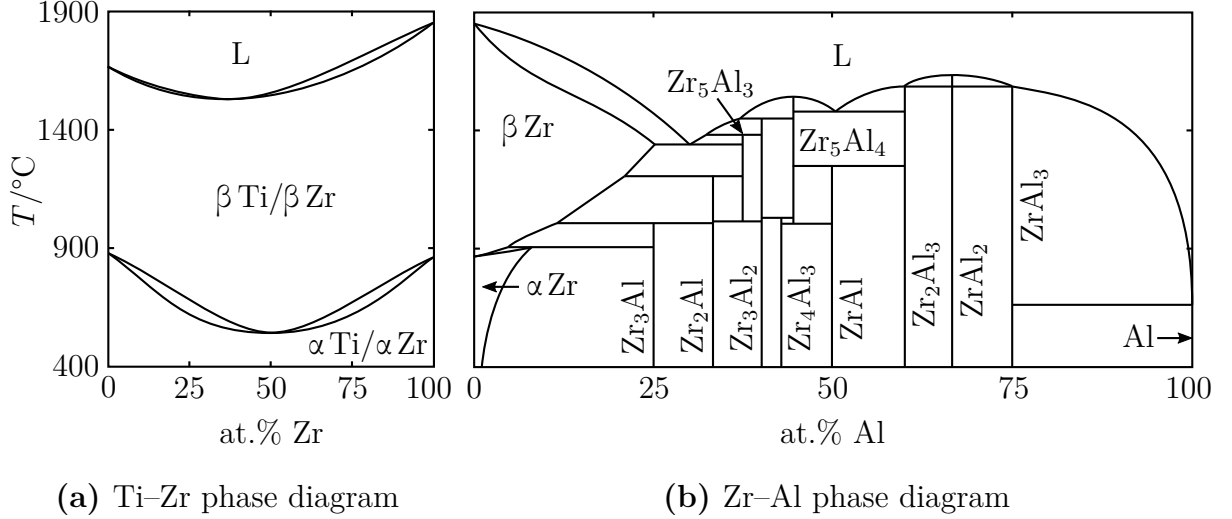


**Figure 2.3:** (a) Complete solid and liquid solubility in the binary Ti–Zr system as given by [15], modified. At 1855 °C, Zr has the highest melting point of the three elements Al, Ti and Zr. (b) Phase diagram for the system Zr–Al according to Fischer and Colinet [16], modified and corrected. In their proposed phase diagram,  $Zr_3Al_2$  was accidentally labeled  $Zr_5Al_3$ . In the Zr–Al system,  $\alpha Zr$ ,  $\beta Zr$  and Al form solid solutions by accommodating foreign atoms. The other ten phases are assumed to be stoichiometric line compounds.

*al.* [5] found hexagonal  $Zr_5Al_3$  to be stable at 1000 °C, as can be seen in the bottom right corner of Figure 2.4(a). This is in contrast to [16], who only reported tetragonal  $Zr_5Al_3$  stable from 1014 °C upwards, as given in Table 2.1.

Wang *et al.* [17] recently developed a thermodynamic description of the Ti–Al–Zr system. Resulting from the calculation of phase diagrams (CALPHAD) in their work, three isothermal sections of the low-Zr part of the ternary system are shown in Figure 2.4(a)–(c). They are for the most part supported by experimental data by [6]. Both at 1200 °C and at 1300 °C, the three-phase field  $\alpha Ti + \beta Ti + \gamma TiAl$  remains at lower Zr contents in calculation than determined in experiment. Adjusting the parameters of the calculations to increase the stability of the  $\alpha$  phase at these temperatures up to higher Al or Zr contents was deemed not possible by the authors. At 1200 °C and 1300 °C, the calculated  $\alpha + \beta$  phase field for the binary Ti–Al side of the ternary system is narrower than in Schuster and Palm’s binary Ti–Al phase diagram [9], compare Figure 2.4(c) and Figure 2.1(a). In the Ti–Al system, for 1200 °C and just above, the uncertainty in relation to the  $\beta$  transus line due to B2-type ordering  $\beta \rightarrow \beta_0$  is discussed in [9].

As opposed to the other ternary alloying elements investigated by [6], Zr appears to at all temperatures partition to the  $\gamma$  phase the most. Only then it partitions to  $\beta Ti$  and least to  $\alpha Ti$ . This trend has been reproduced in the calculations by [17], as can be seen in Figure 2.4(b) and Figure 2.4(c). Therein, the  $\gamma TiAl$  corner of the  $\alpha + \beta + \gamma$  three-phase

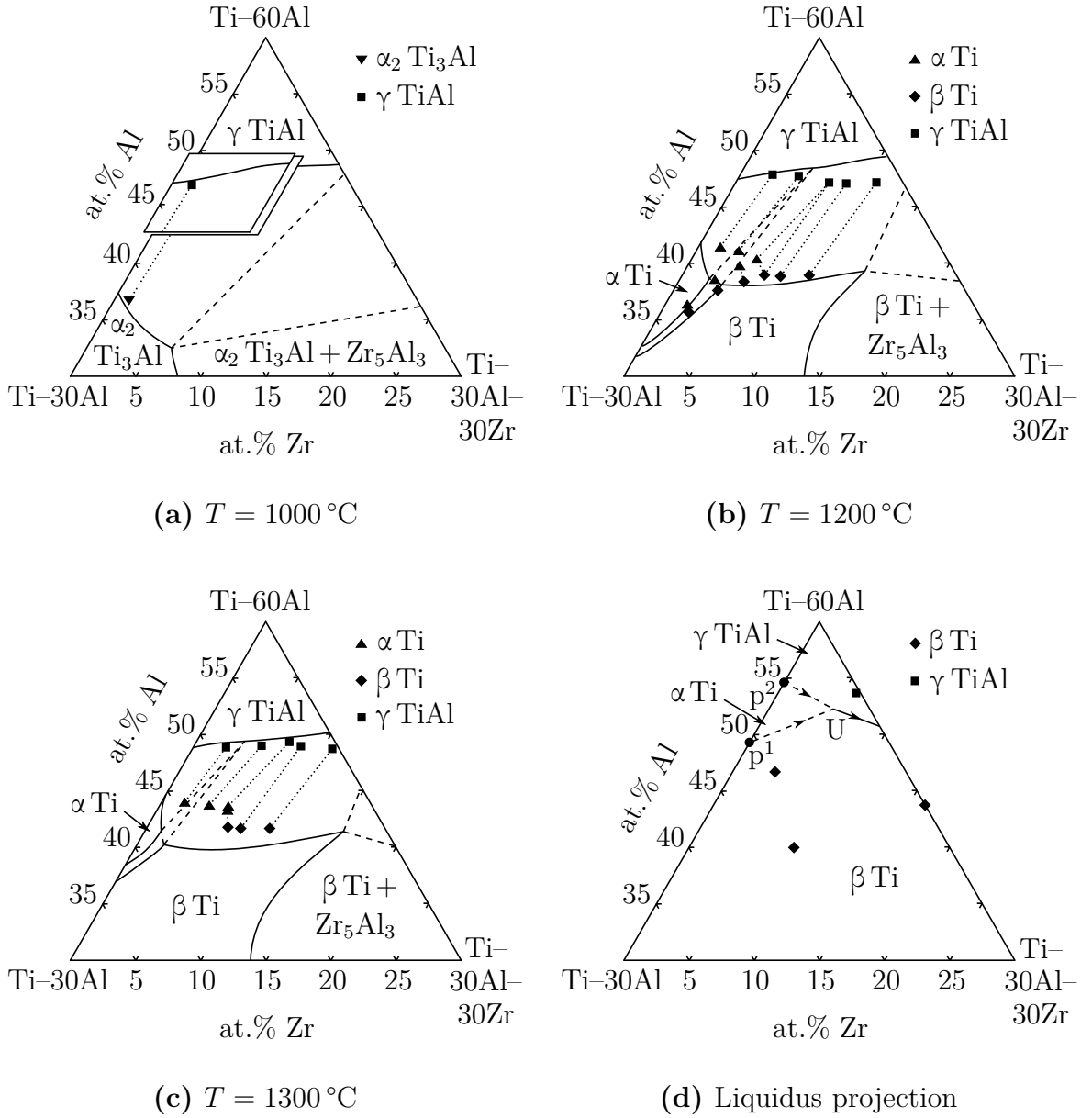


**Figure 2.4:** (a)–(c) Partial isothermal sections of the ternary Ti–Al–Zr system at different temperatures according to [17], modified. Shown are the phase boundaries as calculated via CALPHAD, three-phase fields with dashed lines. Solid markers and dotted tie lines show phase equilibria as experimentally determined by [6]. The cutout in (a) shows the compositional area of interest for this work. Comparing calculation and experiment, note the shifted  $\alpha$  single- and  $\alpha + \beta + \gamma$  three-phase fields. (d) Section of the Ti–Al–Zr system’s liquidus projection as proposed by [12], modified.  $U$  is a ternary peritectic invariant reaction,  $p^1$  and  $p^2$  mark the liquid compositions in the binary peritectic invariant reactions as given in [8], at  $1491\text{ }^\circ\text{C}$  and  $1456\text{ }^\circ\text{C}$  respectively. Arrows point in the direction of falling temperature, the markers indicate investigated alloys and their detected primary phase. Dashed lines signify data extrapolated from the invariant reactions of the binary systems.

triangle is located at the highest Zr contents, the  $\alpha$ Ti corner at the lowest Zr contents. This feature is not present in the calculations by Deng *et al.* [3], which fit the experimental data by [6] slightly worse. At 1000 °C, Hashimoto *et al.* [18] also found that Zr prefers to partition to  $\gamma$  TiAl as opposed to  $\alpha_2$  Ti<sub>3</sub>Al. The partitioning behavior of Zr has an influence on phase transition temperatures. Its preferred partitioning to  $\beta$  Ti as opposed to  $\alpha$  Ti, for example, has been shown to lower the  $\beta$  transus temperature [14].

The research of Abreu *et al.* [12] yielded a liquidus projection of the full Ti–Al–Zr system. Several alloys were analyzed in terms of their microstructure in the as-cast condition. Figure 2.4(d) shows a section of the liquidus projection from 30 at.% to 60 at.% Al and from 0 at.% to 30 at.% Zr. For the ternary invariant reaction U, the equation is  $\text{Liq} + \alpha \text{Ti} \leftrightarrow \beta \text{Ti} + \gamma \text{TiAl}$ , hence it is of peritectic type. Based on microstructural evaluation and on extrapolated CALPHAD data, U was estimated to take place at a liquid composition of Ti–52.0Al–5.0Zr.  $p^1$  and  $p^2$  mark the liquid compositions of the peritectic invariant reactions as given by Witusiewicz *et al.* [8], at 49.4 at.% Al, 1491 °C and 54.7 at.% Al, 1456 °C respectively. It has to be mentioned that according to Schuster and Palm [9], whose binary Ti–Al system is accepted throughout the rest of this work,  $p^2$  is located at 59.0 at.% rather than 54.7 at.% Al. However, this difference is not relevant with respect to the solidification paths of the alloys used in this work, since their Al contents only range up to 49.5 at.%. According to the liquidus projection of Figure 2.4(d), all of the sample material investigated in this work solidifies via the  $\beta$  phase. It has to be mentioned though that Zollinger *et al.* [19] reported a shift from  $\beta$  to  $\alpha$  as the primary solidification phase in some Ti–Al alloys with high O content of about 1 at.%.

Lü *et al.* [20] and Yang *et al.* [5] explicitly state not being able to detect ternary compounds anywhere in the Ti–Al–Zr system, at 800 °C and 1000 °C respectively. In their study on the system’s liquidus projection, Abreu *et al.* [12] found no ternary compounds as well. This is in contrast to earlier research by Sornadurai *et al.* [21], who reported the ternary intermetallic phase Zr<sub>2</sub>TiAl in samples annealed at 1000 °C and 1050 °C. Another intermetallic compound with the composition Ti<sub>2</sub>ZrAl could be detected in a sample annealed at 1000 °C as well [22]. Because of the wide stability range of the  $\beta$  phase at elevated temperatures, the Ti<sub>2</sub>ZrAl and Zr<sub>2</sub>TiAl phases could be ordered structures within  $\beta$  Ti rather than separate intermetallic phases [14]. The compositions of both these proposed phases are far from the compositional ranges looked at in the present work, compare Chapter 1. It is therefore not expected to find them in any of the alloys investigated.

## 2.2.2 Mechanical Properties

Solid solution strengthening of  $\gamma$  TiAl via the addition of Zr is attributed to an asymmetric distortion of the lattice with respect to the  $a$  and  $c$  axes [4]. According to Kawabata *et*

*al.* [2], when keeping the Al content of Ti–50Al constant, 2 at.% to 6 at.% of added Zr decrease both the  $a$  and  $c$  lattice parameters and increase the  $c/a$  ratio. They annealed samples for four-point bend tests for 167 h at 1000 °C and found that alloying with Zr increases bend yield stress over the whole investigated temperature range, from room temperature to 800 °C. Their results also suggest a decrease in bend fracture strain with the addition of Zr. They attributed both these effects, the increased yield strength as well as the reduced ductility, to the increased  $c/a$  ratio and the resulting higher anisotropy of the crystal lattice, which inhibits dislocation mobility. Ambiguous statements were made by the authors about potential grain refining effects of Zr, though they suggest its use as a microalloying element might be beneficial in this respect.

Exactly the opposite of what [2] observed, Tanda *et al.* [23] found an increase in both  $c$  and  $a$  lattice parameters and an overall decrease in  $c/a$  ratio when investigating Ti–50Al with Zr content rising from 0 at.% to 15 at.%. Samples for the investigation of mechanical properties were annealed for 10 h at 1000 °C and air cooled to achieve polycrystalline  $\gamma$  microstructure. When performing Vickers hardness tests, higher hardness values for higher Zr contents were found. The authors attributed this to solid solution hardening. Compared to all other investigated alloys, Ti–50Al–5Zr showed significantly higher plastic strain from room temperature up to 1000 °C during compression testing. It did not undergo brittle fracture at any of the investigated temperatures, as can be seen in Figure 2.5(a). Compressive stress and strain curves for this alloy are shown in Figure 2.5(b). A maximum in yield stress is reached at 700 °C while the maximum fracture strain was found at 200 °C.

A decrease in  $c/a$  ratio with the addition of 5 at.% Zr to Ti–44Al is also what Bresler [1] observed. In his work, it was proposed that Zr acts as an effective solid solution hardener in  $\gamma$  TiAl. However, strain rate jump tests at room temperature showed no improvement of mechanical properties with respect to its addition. The ternary single phase  $\gamma$  alloy displayed increased deformation resistance only at higher temperatures of 750 °C and 900 °C. Additionally, the author found significantly reduced lamellar spacing within  $\alpha_2/\gamma$  colonies when comparing Ti–44Al–5Zr to binary Ti–44Al, both subject to comparable heat treatments. At 900 °C, the creep resistance of the ternary fully lamellar alloy was significantly superior compared to the binary one, as was the deformation resistance obtained from strain rate jump tests.

Appel *et al.* [4] put forward that the site occupancies of the elements in the lattice influence solid solution hardening. In  $\gamma$  TiAl, Zr primarily occupies Ti sites [24], [25], see also Figure 2.1(b). Doi *et al.* [11] investigated alloys containing 2.7 at.% and 6.5 at.% Zr, where in both cases less than 0.5 at.% Zr were located at Al sites. They found that Zr does not substitute Ti atoms in  $\text{Ti}_{\text{Al}}$  antisite defects, instead it displaces Ti from its proper sites to Al ones, thus creating  $\text{Ti}_{\text{Al}}$  defects. As a consequence, high Zr contents have a



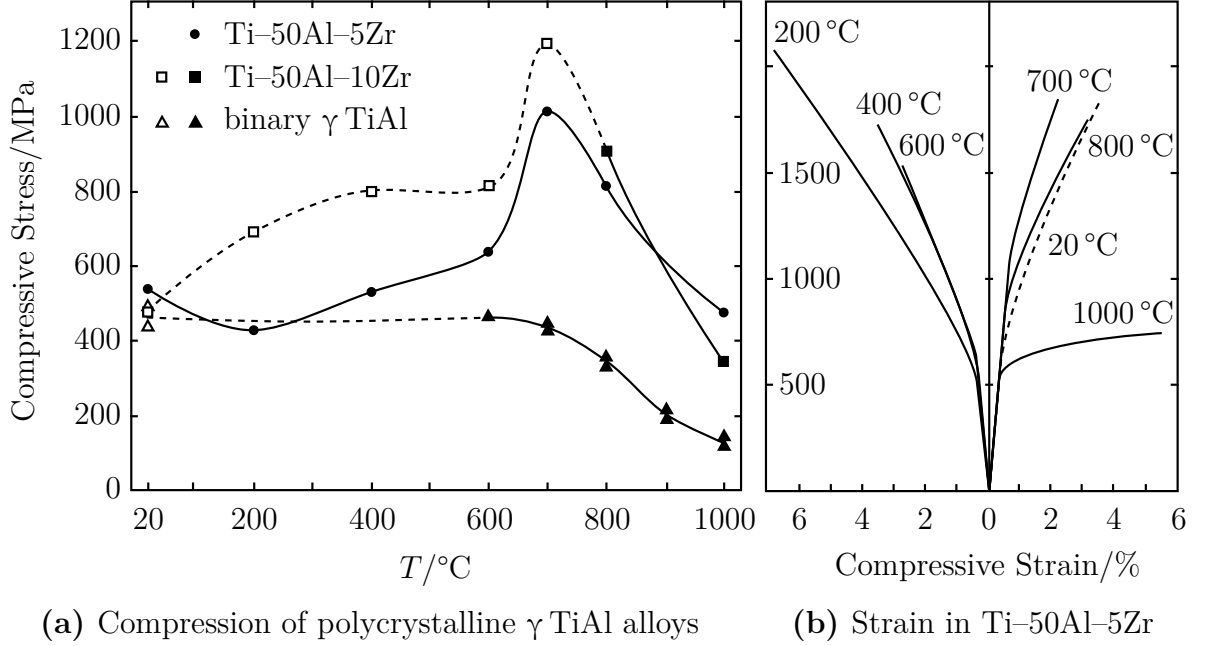


**Figure 2.5:** Both according to [23], modified: (a) Fracture stress (open markers) and 0.2% yield stress (solid markers) for polycrystalline  $\gamma$  TiAl single phase alloys, compression loaded at a strain rate of  $1.7 \times 10^{-4} \text{ s}^{-1}$ . Ti-50Al-5Zr was the only alloy to exhibit non-brittle yield behavior at all investigated temperatures. (b) Compressive stress and strain curves for Ti-50Al-5Zr. Note the maximum fracture strain at 200 °C and maximum yield stress at 700 °C. The curve for 20 °C is indicated with a dashed line to increase readability.

negative influence on the degree of order in the  $\gamma$  phase [11]. Contrary to  $\text{Al}_{\text{Ti}}$  antisite defects, meaning Al atoms located at Ti sites, the lattice distortion provided by  $\text{Ti}_{\text{Al}}$  antisite defects does not contribute much to solution hardening in  $\gamma$  TiAl [4].

Schulz [26] performed room temperature nanoindentation on the  $\gamma$  phase of Ti-Al-Zr alloys. Samples were annealed for 23 h at 1300 °C and furnace cooled to achieve large  $\gamma$  grains. Upon electrochemical polishing, several indents per grain were taken and up to 10 grains were tested per alloy. The average values for hardness and modulus of  $\gamma$  TiAl with single-crystalline behavior are presented in Table 2.2. The hardness of the  $\gamma$  phase appears to increase with Zr content. From a statistical point of view, the apparent increase in modulus might be insignificant when taking into account the standard deviation of the data. Due to the  $c/a$  ratio close to 1 of  $\gamma$  TiAl, EBSD imaging was inconclusive and a relationship between mechanical properties and crystal orientation could not be established. Zambaldi [27] nonetheless showed that the tetragonality of the  $\gamma$  phase can be resolved in EBSD, enabling orientation mapping. Interestingly, alloying 2.1 at.% of Zr decreases Al content in the  $\gamma$  phase, as can be seen in Table 2.2. This can be explained by the displacement of Ti to Al sites and the creation of  $\text{Ti}_{\text{Al}}$  antisite defects described above. In turn, the Al atoms are relocated from  $\gamma$  TiAl to the  $\alpha/\alpha_2$  phase. At 8.0 at.%, Zr appears to

**Table 2.2:** Composition, nanoindentation hardness and modulus of  $\gamma$  TiAl crystallites at room temperature, taken from [26]. Both hardness and modulus seem to increase with alloyed Zr. At least for modulus data, statistical significance might not be given due to overlapping standard deviations.

Alloy	at.% in $\gamma$			in GPa	
	Ti	Al	Zr	Hardness	Modulus
Ti-46.5Al	50.5	49.5	—	$3.49 \pm 0.25$	$161.3 \pm 9.5$
Ti-46.4Al-2.1Zr	49.9	47.6	2.5	$4.22 \pm 0.46$	$170.4 \pm 8.1$
Ti-46.7Al-8.0Zr	44.4	46.9	8.7	$5.03 \pm 0.54$	$177.3 \pm 12.2$

also move Ti atoms from the  $\gamma$  phase to the  $\alpha/\alpha_2$  phase.

In conclusion, the influence of Zr addition on lattice parameters and tetragonality of the  $\gamma$  phase is uncertain. Its positive effect on yield stress over the whole temperature range seems to be agreed upon by most authors though.

### 2.2.3 Oxidation Behavior

Severe oxidation in  $\gamma$  TiAl based alloys starts at 750 °C to 850 °C [28], which is not far from service temperature [4]. Therefore, when looking at new alloys for high-temperature applications, their oxidation behavior has to be considered. Rahmel *et al.* [29] summarized the fundamentals of  $\gamma$  TiAl alloy oxidation that follow. Figure 2.6(a) shows the three main stages of oxidation. Their corresponding oxide scale structures on the surface of the alloy can be seen in Figure 2.6(b). Because of  $\gamma$  TiAl's Al content close to 50 at.%, a protective scale of  $\text{Al}_2\text{O}_3$  can grow on the surface of the sample. This happens during the initial stage A, where a dense layer of  $\text{Al}_2\text{O}_3$  is formed. This layer acts as an effective protection from further oxidation. Since Al diffusion is slow in the substrate, the zone beneath the oxide scale gets depleted of Al. But the similar O equilibrium pressures of the Al oxide/Al and the Ti oxide/Ti systems [30] equally facilitate the formation of a  $\text{TiO}_2$  scale. As other Ti oxides,  $\text{TiO}_2$  is fast growing and poorly protective, the opposite of  $\text{Al}_2\text{O}_3$ . With progressing time or temperature a first breakdown occurs, initially because Al diffusion from the base alloy is outmatched by O diffusion through the oxide. The sample transitions to stage B, where  $\text{TiO}_2$  forms beneath and above the  $\text{Al}_2\text{O}_3$  layer, diminishing the scale's protective capabilities. The further inward and outward growth of  $\text{TiO}_2$  leads to a second breakdown and the beginning of stage C. The remaining  $\text{Al}_2\text{O}_3$  gets dissolved, yielding a disperse scale of mixed  $\text{TiO}_2$  and  $\text{Al}_2\text{O}_3$ . Which of the two oxides dominates, and accordingly, which of the above stages prevails, is determined by the activities of the

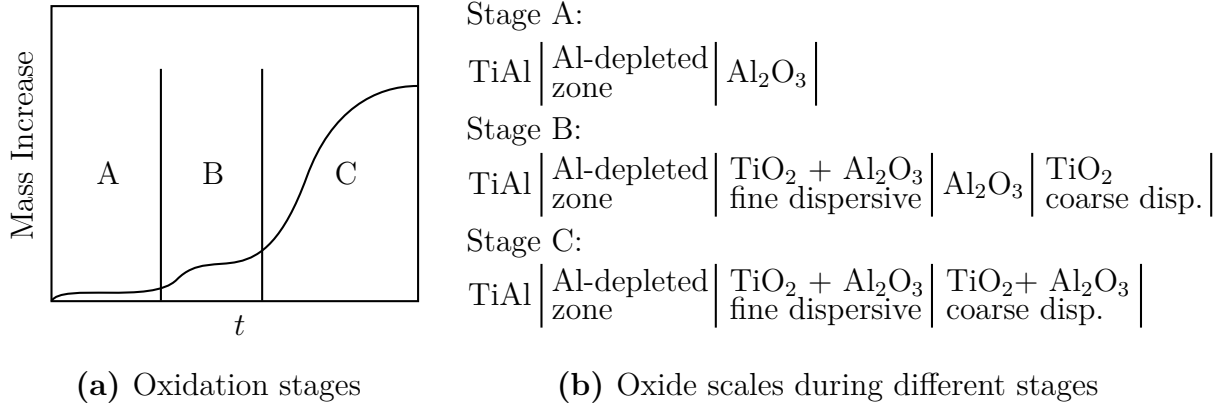


**Figure 2.6:** Both according to [29], modified: (a) Stages of oxidation in  $\gamma$  TiAl based alloys, schematically. With progressing time several breakdowns occur, increasing sample mass through oxidation. (b) Oxide scales during the different stages, with the base alloy on the left and atmosphere on the right.

metals and their oxides. It can thus be changed by alloying.

Not a lot of research has been conducted on the influence of Zr addition on the oxidation behavior of Ti–Al alloys. When compared to binary Ti–50.3Al, Taniguchi *et al.* [31] found improved oxidation performance in a Ti–49.3Al alloy containing 0.09 at.% Zr. This was true for short-term exposure ( $< 100$  h) to pure  $O_2$  at  $927^\circ\text{C}$  and  $1027^\circ\text{C}$  as well as for thermal cycle conditions. Though Zr was enriched neither in the scale nor in the base material, the authors attributed the improvement to a stabilizing effect of Zr on the protective  $Al_2O_3$  scale, not allowing the sample to progress beyond stage A of Figure 2.6(a). They proposed that Zr could slow down the diffusion of O through the  $Al_2O_3$  scale via modification of grain boundary structure or grain size. At  $1077^\circ\text{C}$  and  $1127^\circ\text{C}$ , this stabilizing effect was not present any more and the samples went through all three stages of oxidation. Neither Zr oxide nor ternary compounds of Ti–Zr–O or Al–Zr–O could be detected in any of the samples via X-ray diffraction. Woo and Lee [32] found the oxide scale structures of stage B described by [29] when investigating a Ti–47Al–1.7W–3.7Zr alloy. Their oxidation experiments were done in air for less than 100 h between  $900^\circ\text{C}$  and  $1050^\circ\text{C}$ . During X-ray diffraction however, they detected monoclinic and tetragonal  $ZrO_2$ . For such high Zr contents, this was anticipated by Taniguchi *et al.* [31] and expected to speed up the transport of O through the oxide scale. Shida and Anada [33] found 0.81 at.% of added Zr to behave neutrally with respect to the oxidation properties of a Ti–48.7Al alloy at  $900^\circ\text{C}$ . 100 h oxidation tests were performed in air and compared to binary Ti–48.8Al. The mass increase of the alloyed sample did not differ significantly from the binary one. In conclusion, from present literature a clear trend of the influence of Zr on the oxidation properties of  $\gamma$  TiAl based alloys could not be determined.

# Chapter 3

## Experimental

### 3.1 Sample Material

Sample material was acquired from GFE METALLE UND MATERIALIEN GMBH in Nuremberg, Germany. After vacuum arc remelting and induction skull melting, cylindrical ingots 230 mm in length and 60 mm in diameter were centrifugally cast. They received a hot isostatic pressing (HIP) treatment for 4 h at 200 MPa and 1200 °C. Sample material for the alloys with a nominal Al content of 46.5 at.% was provided in this form. Chemical analysis was performed by GFE METALLE UND MATERIALIEN GMBH as well, using X-ray fluorescence (XRF) spectroscopy, inductively coupled plasma optical emission spectroscopy (ICP-OES) and carrier gas hot extraction (CGHE). The detailed chemical compositions of the ingots can be seen in Table 3.1, for a description of the manufacturing procedures employed refer to [34]. Part of the ingot material was taken and alloyed with either Al or Ti to get an increase or a decrease in Al content. The relative decrease of Zr content caused by this procedure was below 0.5 at.%, its effects are discussed in Section 5.3. The resulting Al variants of the Ti–Al–Zr alloys were remelted four times and provided as buttons approximately 60 mm in diameter and 15 mm in height. The button samples underwent HIP treatment at 110 MPa and 1150 °C for 4 h. For synchrotron

**Table 3.1:** Compositions of the ingot alloy material manufactured via centrifugal casting and further used to prepare the Al variants used in this work. The alloying contents according to chemical analysis are given in at.%, balance is the amount of Ti.

Alloy	Al	Zr	Cu	Fe	Si	C	H	N	O	Cr
Ti-46.5Al-2Zr	46.4	2.1	0.002	0.02	0.01	—	0.04	0.03	0.1	0.006
Ti-46.5Al-4Zr	46.1	4.4	0.007	0.02	0.01	0.02	0.08	0.01	0.1	—
Ti-46.5Al-8Zr	46.7	8.0	0.02	0.03	0.01	—	0.04	0.02	0.09	0.009

measurements (see Section 3.6), cylindrical samples of 20 mm diameter and 10 mm height were manufactured via spark plasma sintering (SPS). The samples were sintered for 3 min at 50 MPa and the temperatures 1350 °C (Ti-46.5Al-2.1Zr), 1360 °C (Ti-46.3Al-4.4Zr) and 1300 °C (Ti-46.8Al-8.0Zr).

## 3.2 Differential Scanning Calorimetry

Cubes of approximately 2 mm in size were cut from the center of the ingots/buttons and the cube edges chamfered. Measurements were carried out on a SETARAM LABSYS EVO differential scanning calorimeter using open (lidless) THEPRO 100  $\mu$ l Al<sub>2</sub>O<sub>3</sub> crucibles. Prior to use, the crucibles were held at 1500 °C for 4 h in an HTM REETZ vacuum oven to remove any residue or grime. During DSC, the samples were heated to 1550 °C and held there for 10 min, before being cooled at a rate of 20 K min<sup>-1</sup>. Ar gas was used for flushing the vacuum chamber. For each alloy, heating rates of 10 K min<sup>-1</sup>, 20 K min<sup>-1</sup> and 40 K min<sup>-1</sup> were used, gained data was exported to text files using SETARAM CALISTO software. The evaluated transition temperatures were extrapolated to a heating rate of 0 K min<sup>-1</sup>, see inset in Figure 3.1. The calculated value was used as equilibrium transition temperature. As shown in Figure 3.1, transition temperatures were evaluated using either peaks or inflection points. Solidus temperature, meaning the highest temperature at which all of an alloy is still solid, was taken to be at the point where the DSC curves deviated from linear leading into a sudden drop. Liquidus temperature, the lowest temperature where pure liquid phase is present at a given chemical composition, was assumed to be at the deepest valley of the DSC curves before the final rise.

## 3.3 Sample preparation

The ingots and buttons of the alloys were cut to smaller-sized specimens using a STRUERS BOD13 diamond cut-off wheel. The ATM BRILLANT 221 cut-off machine was run at 3600 min<sup>-1</sup> with a feed rate of 0.8 mm min<sup>-1</sup>. To reduce scratching by oxide particles from sample surfaces, oxide layers on the sample sides were ground away before preparation. To facilitate unmounting of the finished samples from the mold resin, they were dabbed with STRUERS ANTISTICK. For subsequent wet grinding and polishing, samples were embedded in STRUERS POLYFAST on a STRUERS CITO-PRESS 20. They were then mounted on 6-fold sample holders for preparation on a STRUERS TEGRAMIN grinding machine. First, a leveling step was done on 180 grit SiC paper, followed by a 20 s grind on 1200 grit and three 20 s grinds on 2000 grit SiC paper. Polishing was done for 5 min on a STRUERS MD-CHEM cloth using a 6:1 mixture by volume of STRUERS OP-S and

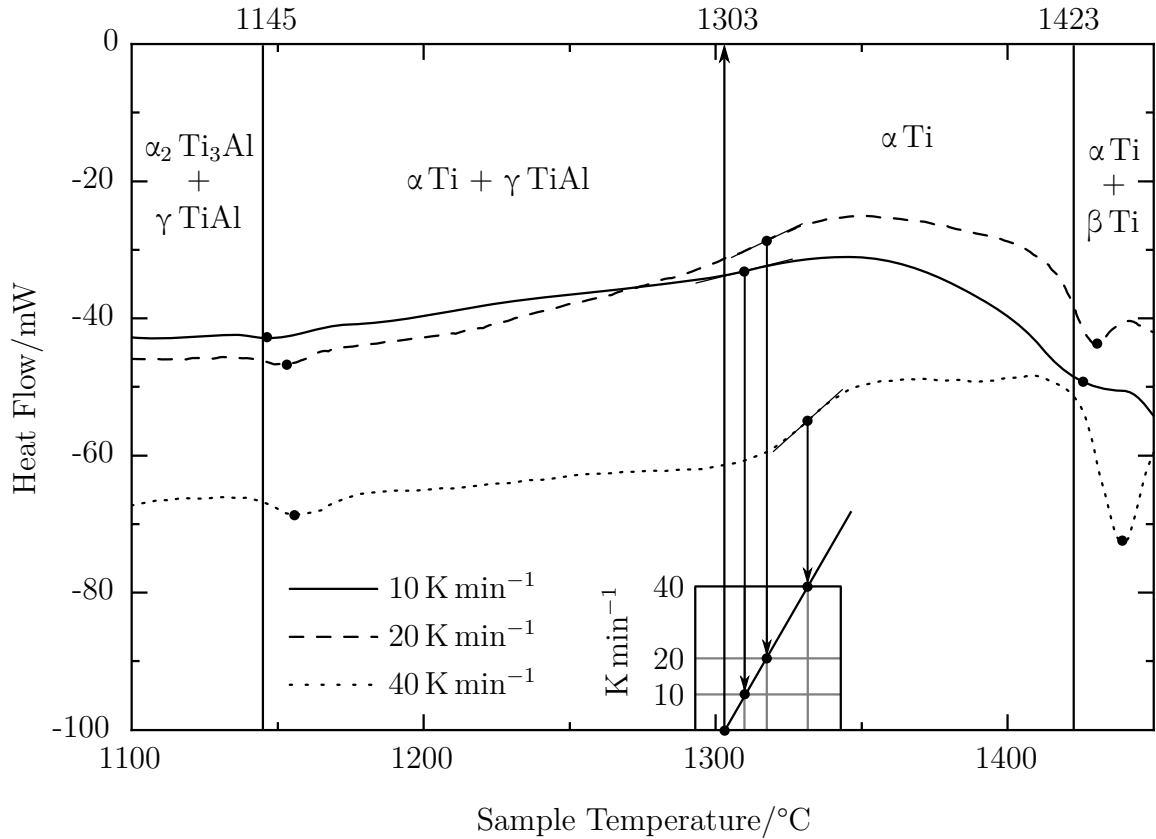


**Figure 3.1:** DSC heating curves for Ti-44.5Al-2Zr. Eutectoid temperature was determined through peaks,  $\alpha$  transus temperature via inflection points. The inset shows the extrapolation used to get an estimate of equilibrium peak temperature. Melting of the sample occurred above 1450 °C.

H<sub>2</sub>O<sub>2</sub>. To remove OP-S silica residue from the polished samples, their surface was rubbed with undiluted liquid hand soap using a gloved finger. The final step consisted in a 10 min run in a BANDELIN SONOREX RK100 ultrasonic cleaner with ethanol as a solvent. The above preparation method for metallography was elaborated by Fleißner-Rieger *et al.* [35].

### 3.4 Heat Treatments and Analysis of Microstructure

10 mm cubes were heat treated in oxidizing atmosphere using a CARBOLITE GERO RHF 1600 high temperature furnace. Heat treatment temperatures were chosen taking into account the results of DSC analysis for an approximate position of phase transition lines. Holding times for the samples were the following: 60 min at 1320 °C and 1390 °C, 30 min at 1430 °C and 15 min at 1470 °C. At high temperatures, holding time was limited by quick oxidation of the samples high in Zr (see Section 4.5). The samples were then water quenched to freeze their microstructure at elevated temperature. Next, they were cut in half and prepared according to the procedure described in Section 3.3. Microstructure

characterization was done using polarized light microscopy with linearly polarized light on a ZEISS AXIO IMAGER 2, the analyzer opened to  $90.65^\circ$ . EC EPIPLAN-NEOFLUAR objectives and an AXIOCAM ERC 5S camera by ZEISS were used. Additionally, some samples were analyzed in BSE contrast on a TESCAN CLARA SEM with an acceleration voltage of 20 kV. Energy-dispersive X-ray spectroscopy (EDX) was carried out on using the same SEM and an X-MAX detector by OXFORD INSTRUMENTS. Their AZTEC software was used to determine the composition of unknown phases.

### 3.5 X-ray Diffraction

Polished samples (see Section 3.3) were released from their molds and investigated in a BRUKER AXS D8 ADVANCE diffractometer using a locked coupled, continuous scan and a SOL-X detector. The rotating samples were irradiated with a Cu  $K_\alpha$  beam with a source voltage of 40 kV and a source current of 40 mA. Scanned were  $2\theta$  angles of  $11^\circ$  to  $82^\circ$  with a step size of  $0.02^\circ$  and a step interval of 2.4 s. Gained diffraction data was processed in TOPAS, a structure analysis software by BRUKER. The diffraction pattern was Rietveld fitted between  $30^\circ$  and  $70^\circ$  assuming the presence of  $\alpha_2$ ,  $\beta_o$  and  $\gamma$  phase in the sample. To account for any preferred orientation of crystallites and thus achieve a better fit, a spherical harmonics approach was used. Low-order harmonics were tried first, gradually moving to higher-order harmonics until a satisfactory fit was achieved. The determined phase fractions were used together with data from polarized light microscopy, synchrotron X-ray diffraction and DSC to construct the experimental phase diagrams of Section 4.4.

As was described by Doi *et al.* [11], samples containing  $\gamma$  TiAl and  $\alpha_2$  Ti<sub>3</sub>Al display some peaks that typically overlap in XRD patterns. The  $\gamma$  TiAl (222) and  $\alpha_2$  Ti<sub>3</sub>Al (004) peaks, for example, are usually found at the same  $2\theta$  angles. The (200) and (002) peaks of the  $\gamma$  phase can be used to investigate its  $c/a$  ratio. They overlap for low tetragonality, meaning  $c/a \approx 1$ . The information above was taken into account when evaluating the diffraction data obtained in this work.

### 3.6 *In-situ* High-Energy X-ray Diffraction

Three alloys were investigated using high-energy X-ray diffraction at the PETRA III facility of Deutsches Elektronen-Synchrotron (DESY) in Hamburg, Germany. At the P07 High Energy Materials Science beamline samples were irradiated in transmission geometry with a beam energy of 87.1 keV, corresponding to a wavelength of  $0.142 \text{ \AA}$ . An XRD 1621 digital flat panel detector from PERKIN ELMER was used to record in-situ diffraction patterns at a distance of about 1750 mm from the sample. Rectangular cuboids with a

length of 10 mm and a square section of 25 mm<sup>2</sup> were cut from the SPS cylinders described in Section 3.1. A piece of Ta foil was spot welded to the side of each sample under Ar atmosphere. The aim was to provide a diffusion barrier between the investigated alloy and the type B thermocouple. The thermocouple was spot welded on top of the Ta foil and used for temperature control during heating of the sample. Heating up to at least solidus temperature was planned, it was thus expected to get some amount of liquid phase toward the end of the experiment. To protect the hollow connecting rods of the TA INSTRUMENTS 805A/D dilatometer, thin Mo discs with a diameter of 8 mm were glued to the ends of the samples to prevent the liquid metal from wetting the rods and solidifying on them. It was found that using Mo discs thinner than 0.5 mm was necessary to prevent electromagnetic coupling with the induction coil and interference with temperature control of the sample. To reduce Al losses and its subsequent deposition on the thermocouple during heating, measurements were carried out under Ar atmosphere instead of vacuum.

The samples were inductively heated at maximum heating rate from room temperature up to 1100 °C, where they were held for 5 min. They were then heated at a rate of 2 K min<sup>-1</sup> up to 1200 °C. From there, the heating rate was changed to 20 K min<sup>-1</sup>. The samples were heated until solidus temperature, where the experiment was canceled manually upon melting of the sample. One 2D detector image of the diffraction pattern was taken every 10 s. Figure 3.2(a) shows an example of such a detector image displaying Debye-Scherrer rings for the alloy Ti-46.3Al-4.4Zr at room temperature. Each ring results from the diffractions of a single family of crystallographic planes  $\{hkl\}$ . To get plots of intensity over  $2\theta$ , these Debye-Scherrer rings were integrated with FIT2D software by Hammersley [36]. For easier interpretation of the plots, they were compiled frame by frame into a video using a program written specifically for this purpose in PYTHON. Transition temperatures were obtained from the appearance or disappearance of peaks on these videos. After choosing appropriate starting parameters, phase fractions at all temperatures were automatically determined by Rietveld refinement using the software MAUD [37]. With the appearance of liquid phase in the sample, a diffuse ring becomes visible on the 2D detector images, see Figure 3.2(b). The temperature where this ring first appeared was taken to be the solidus temperature of the alloy.

### 3.7 Nanoindentation

To increase the size of the  $\gamma$  grains for nanoindentation, 10 mm cubes were held for 23 h in atmosphere at 1300 °C in a CARBOLITE GERO RHF 1600 high temperature furnace with following furnace cooling. Figure 3.3(a) shows the microstructure of the alloy after this heat treatment. The cubes were then cut in half, embedded in BUEHLER PROBEMET



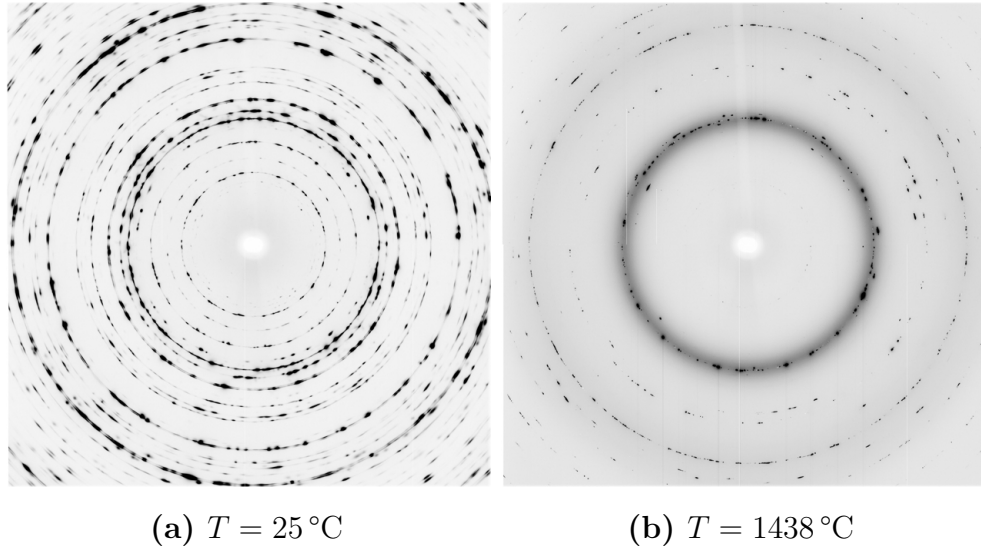


**Figure 3.2:** (a) Exemplary synchrotron diffraction pattern for temperatures below solidus temperature. (b) Above solidus temperature, the onset of melting results in a diffuse ring becoming visible on the diffraction pattern. Both patterns are for Ti-46.3Al-4.4Zr. Regarding the compositions of the alloys used for synchrotron measurements, see Section 3.1.

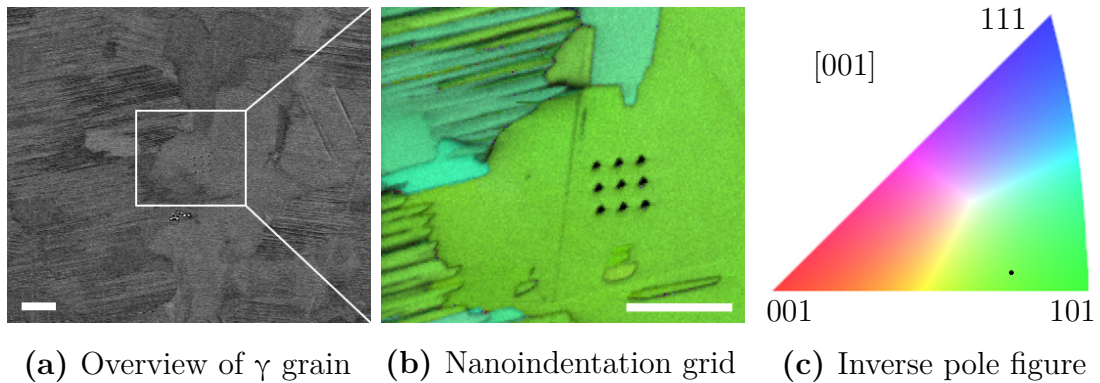


**Figure 3.3:** Scale bar length is  $20\text{ }\mu\text{m}$ . (a) SEM image taken in BSE mode. The microstructure of the Ti-46.5Al-4Zr sample used for nanoindentation was comprised of large  $\gamma$  grains and  $\alpha_2 + \gamma$  lamellae. (b) EBSD image of the indented  $\gamma$  grain visible in (a). Shown are the inverse pole figure (IPF) map in color, giving crystal orientation, and the image quality (IQ) in grayscale. (c) IPF for  $\gamma$  TiAl in  $[001]$  direction. The dot marks the crystal orientation of the  $\gamma$  grain shown in (b), which corresponds to  $[11\ 1\ 16]$ .

on a STRUERS CITO-PRESS 20 and ground according to the specifications in Section 3.3. The samples were electrolytically polished on a STRUERS LECTROPOL 5 using STRUERS A3 electrolyte at room temperature. The used voltage was 36 V, the electrolyte flow rate set to 20 for 24 s. The mask used had an opening 2 cm<sup>2</sup> in size. Immediately upon finishing the etching process, samples were flushed with water and then with acetone.

Nanoindentation of selected  $\gamma$  grains was done on a KLA NANO INDENTER G200 with a diamond Berkovich tip. Continuous stiffness measurement (CSM) [38] was employed, where during measurement contact force and penetration are recorded continuously. To this end, an oscillation of 2 nm amplitude and a frequency of 45 Hz was superimposed on the indenter tip movement. Maximum indentation depth was 200 nm, while the range from 170 nm to 190 nm was used for the evaluation of hardness and modulus. Indentation strain rate was constant at 0.05 s<sup>-1</sup> and a Poisson's ratio of 0.3 was assumed. Measurements and evaluation were performed in NANOSUITE software by KLA and data exported to MICROSOFT EXCEL spreadsheets for further handling. After nanoindentation, the orientation of the indented grains was determined through EBSD using a FEI VERSA 3D DUAL BEAM focused ion beam (FIB) workstation and the attached SEM. Imaging was done at a source voltage of 30 kV and with a HIKARI XP EBSD camera. TEAM and OIM ANALYSIS software by EDAX was used for exporting and analyzing EBSD data. Figure 3.3(b) shows an EBSD image of an exemplary  $\gamma$  grain and the 3 × 3 grid of nanoindents taken thereupon. The derived IPF can be seen in Figure 3.3(c).

# Chapter 4

## Results

### 4.1 Ti–Al–2Zr

#### 4.1.1 Microstructural Characterization

The microstructure of Ti–Al–2Zr alloys heat treated at temperatures 1320 °C, 1390 °C and 1470 °C and then water quenched can be seen in Figure 4.1. The arrangement of the polarized light micrographs is analogous to the way they are placed in the isopleth of Figure 4.9(b): Al content rising from left to right, temperature from bottom to top. Apparent white spots on the sample surface are residual silica particles from polishing with STRUERS OP-S. As was found out, they can be prevented by thoroughly cleaning the samples with pure liquid hand soap after polishing, as described in Section 3.3. Any hair-like cracks visible in the micrographs are quench fractures. In the following paragraphs, the letters in parentheses refer to the subfigures of Figure 4.1.

At 1320 °C,  $\alpha$ Ti is stable up to Al contents of at least 44.5 at.% (k)–(l),  $\gamma$  TiAl starts to appear at 46.5 at.% Al (m). No  $\alpha_2$  phase but pure  $\gamma$  phase is left at 49.5 at.% Al (o). At 1390 °C and 42.5 at.% Al (f), the microstructure does not resemble single-phase microstructure (k) any more. The two phases present are  $\alpha_2$  and  $\beta_o$ . At 44.5 at.% Al (g), it looks like a transformation to  $\alpha + \beta$  is about to happen. Compared to 1320 °C, the  $\alpha$  single phase region is shifted to 46.5 at.% and 48.0 at.% Al at 1390 °C (h)–(i). The speckled, rosette-shaped grains visible in these two micrographs are  $\gamma$  TiAl formed during massive transformation at high cooling rates [4]. They appear mostly on the boundaries and triple points of  $\alpha/\alpha_2$  grains and are not present at heat treatment temperature. At 49.5 at.% Al and 1390 °C (j),  $\alpha$ Ti and  $\gamma$  TiAl can be found. The highest heat treatment temperature 1470 °C was close to or above the solidus temperature for most of the samples. In each of them, indications for the presence of liquid phase were found. While the microstructure at 42.5 at.% Al (a) is comprised of  $\beta_o$  only, liquid phase was detected at the sample edges.

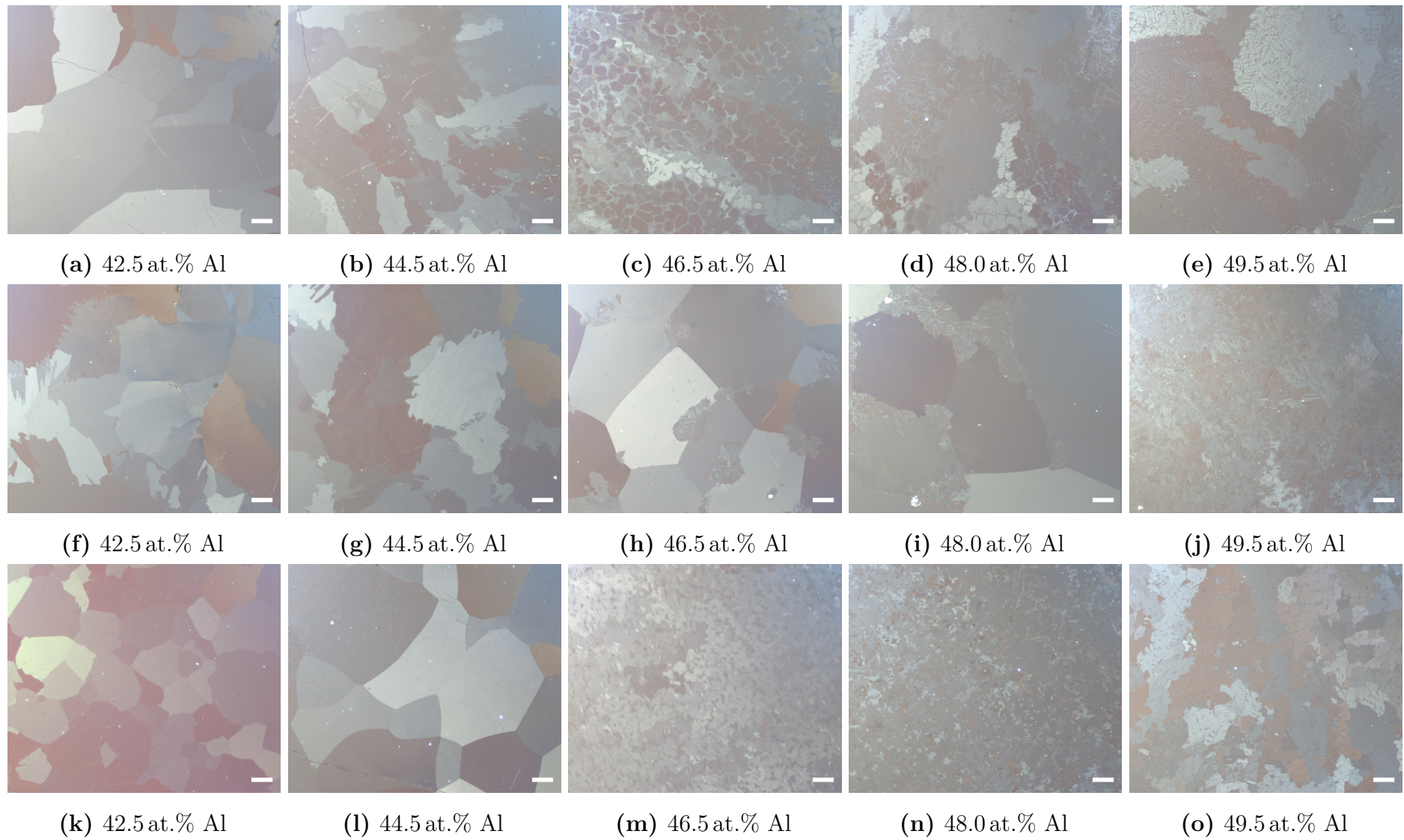
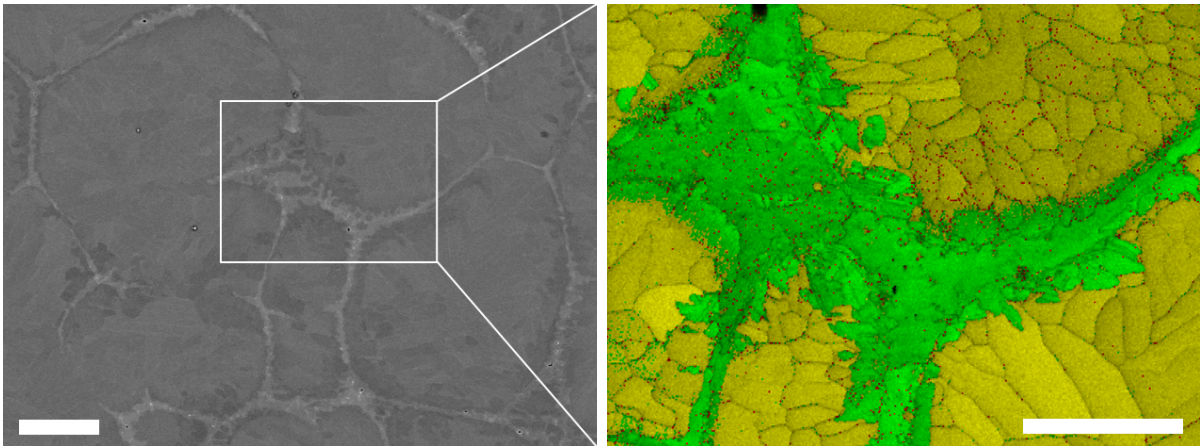


**Figure 4.1:** Polarized light micrographs of Ti-Al-2Zr at (a)–(e) 1470 °C, (f)–(j) 1390 °C and (k)–(o) 1320 °C. Scale bar length is 200 μm.

At 44.5 at.% Al,  $\alpha$  as well as  $\beta$  phase are present at the heat treatment temperature of 1470 °C (b). This temperature seems to coincide with the solidus temperature, since the sample is noticeably infiltrated by liquid phase from the edges inward. A small fraction of liquid phase can be seen in the bottom right corner of the micrograph. The alloys with 46.5 at.%, 48.0 at.% and 49.5 at.% Al (c)–(e) show large volume fractions of liquid phase, though with polarized light microscopy it was not possible to detect the phases present upon melting. Figure 4.2(a) shows a BSE SEM image of the sample shown in Figure 4.1(c). As can be seen from the EBSD image in Figure 4.2(b), it is comprised of  $\alpha_2$  grains surrounded by liquid phase that solidified as  $\gamma$  TiAl.

### 4.1.2 DSC Analysis

To correctly connect peak information with occurring phase transitions in the sample, the DSC results were evaluated in close relation to the microstructural investigations of Section 4.1.1. The DSC curves for the Al variants of Ti–Al–2Zr are shown in Figure 4.3. The transition temperatures for the three different heating rates 10 K min<sup>-1</sup>, 20 K min<sup>-1</sup> and 40 K min<sup>-1</sup> were evaluated as described in Section 3.2. From these values, the transition temperatures for thermodynamic equilibrium were extrapolated. All of the data, the measured transition temperatures as well as the calculated values for 0 K min<sup>-1</sup>, are presented in Table 4.1. The equilibrium peak temperatures are also marked by vertical bars in Figure 4.3. For clearness of presentation, the phase fields and transitions were not labeled within the diagrams but can be read from Table 4.1.



(a) Ti-46.5Al-2Zr quenched from 1470 °C (b) High-temperature  $\alpha + L$  microstructure

**Figure 4.2:** (a) 20 kV SEM image of a Ti-46.5Al-2Zr sample water quenched from 1470 °C, taken in BSE mode. (b) Phase contrast EBSD image of the area marked in (a). Visible are  $\alpha_2$  grains (yellow) surrounded by liquid phase that solidified as  $\gamma$  TiAl (green). Scale bar length is 50  $\mu$ m for both images.

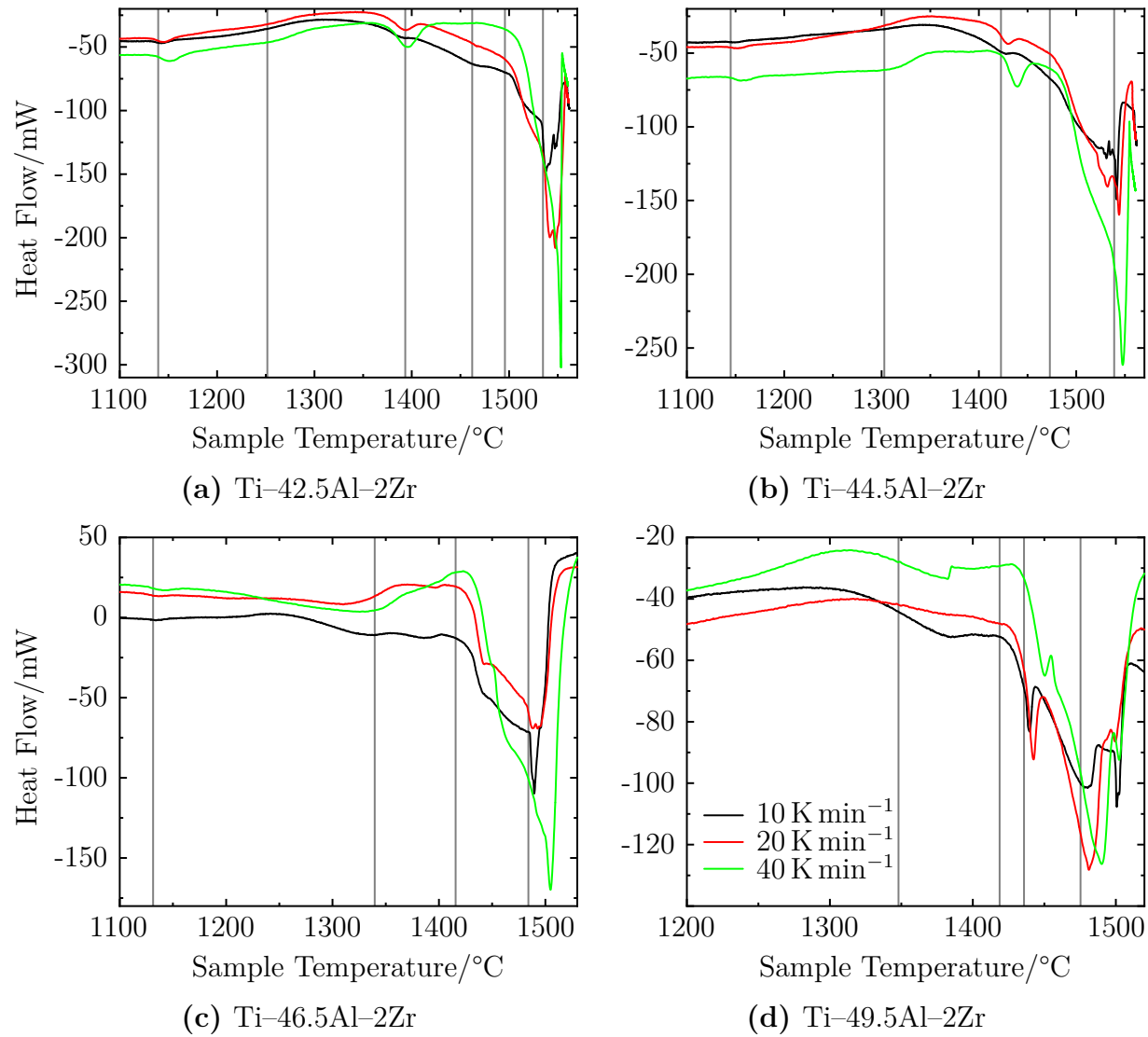


**Figure 4.3:** DSC curves for different Al concentrations of Ti-Al-2Zr. Vertical bars mark equilibrium peak temperatures for 0 K min<sup>-1</sup>.

**Table 4.1:** DSC transition temperatures for different heating rates  $\dot{T}$ . An asterisk signifies that the finite heating rates do not show a trend and the lowest of the above values was used for thermodynamic equilibrium ( $\dot{T} = 0$ ). For liquidus behavior of Ti-46.5Al-2Zr, see text.

Alloy	$\dot{T}/\text{K min}^{-1}$	Transition Temperature/ $^{\circ}\text{C}$						
		$\alpha_2 + \gamma \rightarrow \alpha + \gamma$	$\alpha + \gamma \rightarrow \alpha$	$\alpha \rightarrow \alpha + \beta$	$\alpha + \beta \rightarrow \beta$	$\alpha + \beta \rightarrow \beta + \text{L}$	$\beta \rightarrow \beta + \text{L}$	$\beta + \text{L} \rightarrow \text{L}$
Ti-42.5Al-2Zr	40	1151.2	1277.0	1396.1	1462.1	—	1496.7	1553.7
	20	1145.8	1263.6	1394.5	1467.0	—	1495.7	1547.0
	10	1142.2	1258.3	1394.1	1470.6	—	1499.9	1538.1
	0	1139.5	1251.6	1393.3	1462.1*	—	1495.7*	1534.8
Ti-44.5Al-2Zr	40	1155.6	1331.5	1439.7	—	1478.1	—	1548.0
	20	1153.1	1317.5	1429.6	—	1477.3	—	1544.3
	10	1146.2	1309.8	1427.6	—	1473.3	—	1540.7
	0	1145.0	1302.8	1422.6	—	1472.9	—	1538.9
		$\alpha_2 + \gamma \rightarrow \alpha + \gamma$	$\gamma \rightarrow \alpha + \gamma$	$\alpha + \gamma \rightarrow \alpha$	$\alpha + \gamma \rightarrow \alpha + \gamma + \text{L}$	$\alpha \rightarrow \alpha + \text{L}$	$\alpha + \gamma + \text{L} \rightarrow \alpha + \text{L}$	$\alpha + \text{L} \rightarrow \text{L}$
Ti-46.5Al-2Zr	40	1142.9	—	1357.9	—	1425.5	—	(1505.2)
	20	1137.5	—	1346.6	—	1420.4	—	(1494.0)
	10	1134.1	—	1345.2	—	1418.2	—	(1489.7)
	0	1131.4	—	1339.6	—	1415.7	—	(1484.1)
Ti-49.5Al-2Zr	40	—	1356.1	—	1428.1	—	1450.3	1491.0
	20	—	1353.6	—	1424.0	—	1442.5	1481.1
	10	—	1349.2	—	1420.7	—	1439.7	1480.2
	0	—	1348.0	—	1418.7	—	1435.8	1475.3

In Ti–Al–2Zr, the temperature of the eutectoid transformation  $\alpha_2 + \gamma \rightarrow \alpha + \gamma$  appears to be about 1140 °C. At liquidus temperature,  $\beta$  phase is present up to an Al content of 44.5 at.%. It is unclear whether the sample with 46.5 at.% Al displays  $\alpha$  Ti or  $\beta$  Ti as the last phase before liquidus temperature. For a detailed discussion of this, see Section 5.3. From 49.5 at.% onward melting takes place via the  $\alpha$  phase. Note that the transition  $\alpha + \beta \rightarrow \beta + L$  proposed for Ti–44.5Al–2Zr is thermodynamically not possible in ternary systems. As is discussed in Section 5.3 as well, the alloy has to pass through a three phase region of  $\alpha + \beta + L$  for the  $\alpha$  phase to be able to dissolve completely. That such a three phase region could not be detected in the DSC measurements for the alloy containing 44.5 at.% Al, might be due to a very narrow temperature stability range. An isoplethal (constant composition) section for Ti–Al–2Zr based on the microscopy and DSC data is proposed in Figure 4.9(b).

### 4.1.3 High-Energy X-ray Diffraction

The transition temperatures for Ti–46.5Al–2.1Zr found during synchrotron investigations are given in Table 4.2. The formation of  $\beta$  phase at around 1368 °C, very close to solidus temperature, could be detected. The eutectoid temperature was determined from the disappearance of the  $\alpha_2$  Ti<sub>3</sub>Al superstructure reflex at 1146 °C, above the transition temperature in binary Ti–Al. Since the synchrotron data for Ti–46.5Al–2.1Zr do not agree with the findings from other investigation methods, the diffraction spectra and phase fraction diagrams determined during high-energy XRD are not reproduced here.

## 4.2 Ti–Al–4Zr

### 4.2.1 DSC Analysis

DSC measurements for Ti–46.5Al–4Zr were performed and evaluated according to the procedures described in Section 3.2. The DSC curves found for this alloy can be seen in Figure 4.4. Equilibrium transition temperatures are marked by vertical bars. The transition

**Table 4.2:** Phase transition temperatures for a Ti–46.5Al–2.1Zr alloy manufactured via SPS, determined via high-energy XRD.

Transition Temperature/°C			
$\alpha_2 + \gamma \rightarrow \alpha + \gamma$	$\alpha + \gamma \rightarrow \alpha$	$\alpha \rightarrow \alpha + \beta$	$\alpha + \beta \rightarrow \alpha + \beta + L$
1146	1331	1368	1381



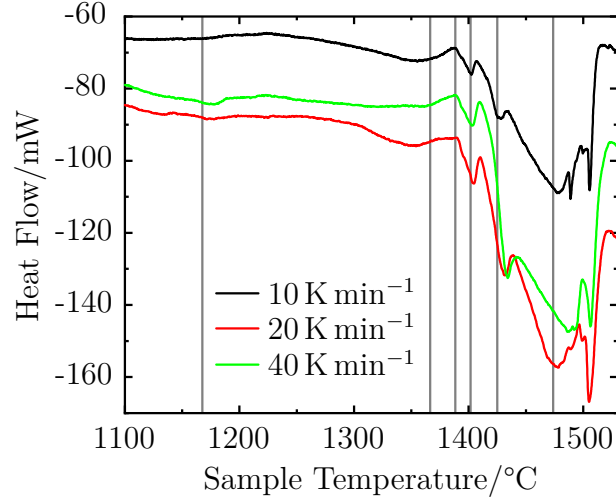


**Figure 4.4:** DSC curves at different heating rates for Ti-46.5Al-4Zr. Vertical bars mark equilibrium peak temperatures for  $0 \text{ K min}^{-1}$ .

temperatures and their supposed phase transformations are given in Table 4.3. The Al variants for Ti-Al-4Zr were investigated via DSC by TU BERGAKADEMIE FREIBERG. Peak analysis was done for curves recorded at a heating rate of  $20 \text{ K min}^{-1}$ . Evaluated phase transition temperatures for all Al contents are marked by dots in Figure 4.9(c).

## 4.2.2 Microstructural Characterization

The microstructure characterization for Ti-Al-4Zr via polarized light microscopy was less conclusive than for the alloys containing 2 at.% Zr. At the heat treatment temperatures  $1390 \text{ }^\circ\text{C}$ ,  $1430 \text{ }^\circ\text{C}$  and  $1470 \text{ }^\circ\text{C}$ , liquid phase was present in most of the investigated alloys. In the following paragraph, the letters in parentheses refer to the subfigures of Figure 4.5, which shows the polarized light micrographs of heat treated and water quenched samples.

**Table 4.3:** DSC transition temperatures at different heating rates for Ti-46.5Al-4Zr. The values for  $\dot{T} = 0 \text{ K min}^{-1}$ , representing thermodynamic equilibrium, were extrapolated. An asterisk signifies that the individual heating rates do not show a trend and the lowest of the above values was used instead.

$\dot{T}/\text{K min}^{-1}$	Transition Temperature/ $^\circ\text{C}$					
	$\alpha_2 + \gamma \rightarrow \alpha + \gamma$	$\rightarrow \alpha$	$\rightarrow \alpha + \text{L}$	$\rightarrow \alpha + \beta + \text{L}$	$\rightarrow \beta + \text{L}$	$\rightarrow \text{L}$
40	1177.5	1372.1	1389.2	1403.1	1434.6	1486.0
20	1172.8	1366.4	1390.2	1404.5	1431.7	1478.3
10	1169.8	1377.4	1388.3	1401.7	1426.4	1477.5
0	1167.5	1366.4*	1388.3*	1401.7*	1425.0	1473.3

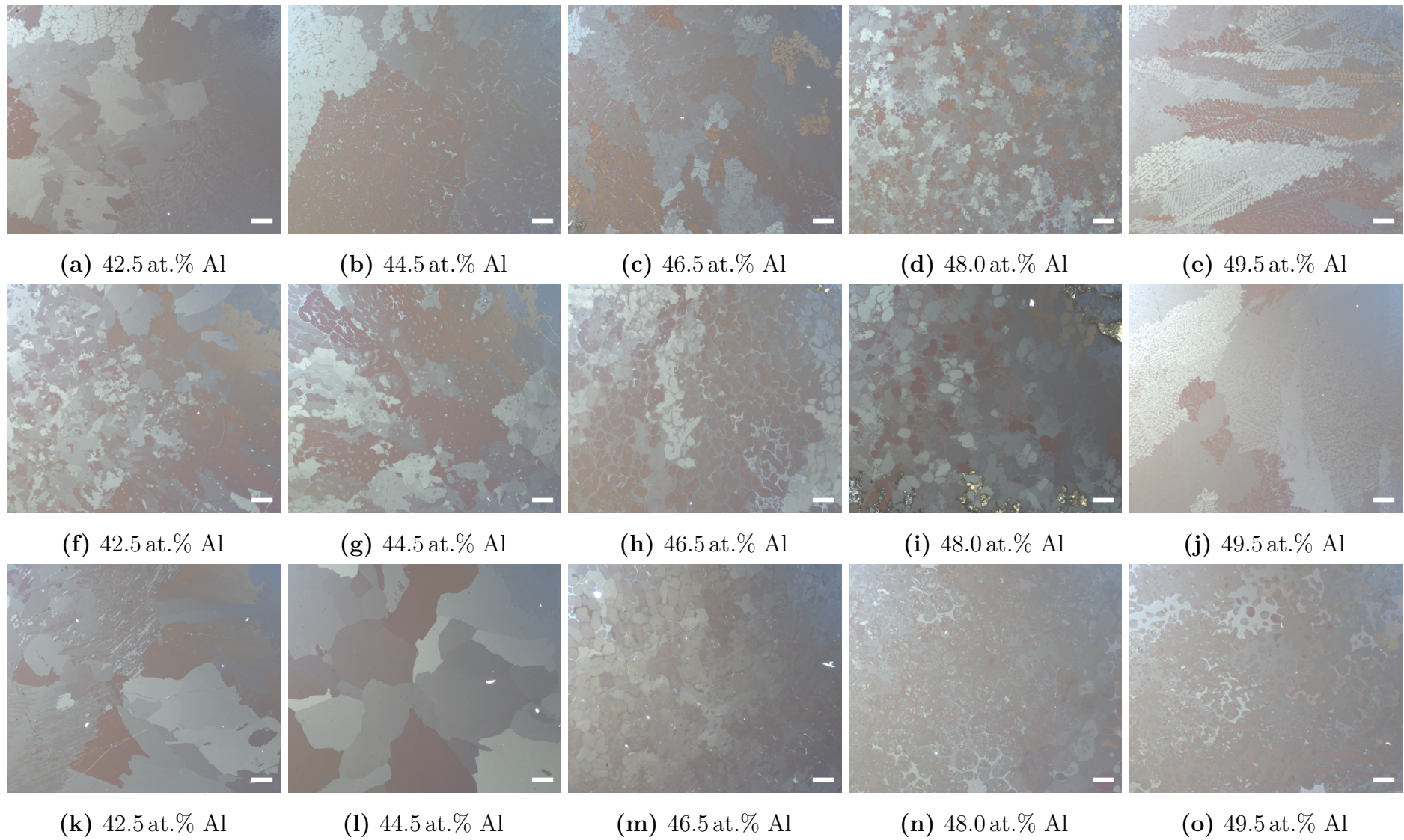
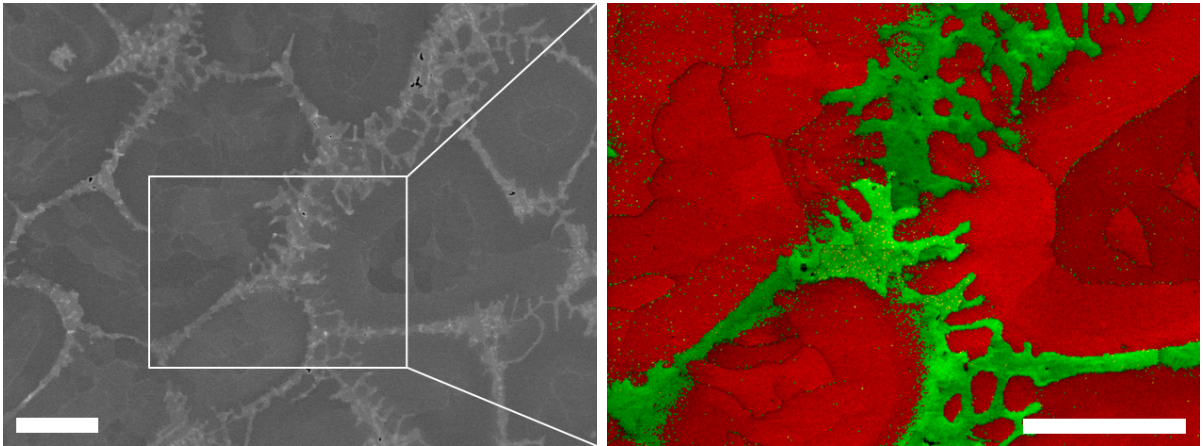


**Figure 4.5:** Polarized light micrographs of Ti-Al-4Zr at (a)–(e) 1470 °C, (f)–(j) 1430 °C and (k)–(o) 1390 °C. Scale bar length is 200  $\mu\text{m}$ .

The first heat treatment temperature of 1390 °C is above the solidus temperature for the Al contents 46.5 at.% to 49.5 at.%, as can be seen from the liquid phase in the micrographs (m)–(o). At lower Al contents (k)–(l), the microstructure does not look as if it only consists of a single phase. The phases present are likely to be  $\alpha_2$  and  $\beta_0$ . For a discussion of the needle-like structures in Figure 4.5(k), refer to Section 5.1. At 1430 °C, liquid phase starts to appear at 42.5 at.% Al (f). From 46.5 at.% Al onward, samples are clearly above solidus temperature (h)–(j). The solid phase could not be identified in polarized light microscopy. Figure 4.6(a) shows a SEM image of Ti–46.5Al–4Zr water quenched from 1430 °C. The phase contrast of its EBSD image in Figure 4.6(b) clearly shows the presence of  $\alpha$  and liquid phase at heat treatment temperature. When taking into account DSC results, the sample with 42.5 at.% Al (f) should be in the  $\beta$  single-phase field at 1430 °C. However, the micrograph shows a very inhomogeneous microstructure which is discussed in Section 5.1 in more detail. Liquid phase could be detected in all of the investigated samples at 1470 °C (a)–(e). The sample with 49.5 at.% Al even showed fully dendritic microstructure, indicating that it melted completely and resolidified. A theory on how water quenching of a sample heat treated above liquidus temperature is possible is given in Section 5.1.

### 4.2.3 Conventional and High-Energy X-ray Diffraction

The signal-to-noise ratio in diffraction patterns for samples which were quenched while partially molten is significantly worse than for non-molten samples. In this work, X-ray



(a) Ti–46.5Al–4Zr quenched from 1430 °C (b) High-temperature  $\alpha + L$  microstructure

**Figure 4.6:** (a) 20 kV SEM image of a Ti–46.5Al–4Zr sample water quenched from 1430 °C, taken in BSE mode. (b) Phase contrast EBSD image of the area marked in (a). Visible are  $\alpha_2$  grains (red) surrounded by liquid phase that solidified as  $\gamma$  TiAl (green). Scale bar length is 50  $\mu\text{m}$  for both images.

diffraction was done for Ti–Al–4Zr alloys heat treated below their solidus temperature. Table 4.4 gives the phase fractions evaluated via Rietveld analysis. As is described in Section 5.3, these are not useful in constructing isopleths via the lever rule, because tie lines of ternary systems do not generally lie all within one plane. It can be observed that at 1200 °C, the alloy with 49.5 at.% Al is the only one solely comprised of  $\gamma$  phase. The sample with 42.5 at.% Al was in the  $\alpha$  single-phase region during heat treatment at 1320 °C. For all other investigated samples,  $\alpha/\alpha_2$  as well as  $\gamma$  phase were detected in XRD spectra. Why the low amounts of  $\beta_o$  phase are insignificant is described in Section 5.4. At the heat treatment temperatures of Table 4.4, no  $\beta_o$  phase could be found in other investigations.

The phase transition temperatures of Ti–46.3Al–4.4Zr measured by means of synchrotron radiation are given in Table 4.5. The solidus temperature at 1400 °C is in good agreement with the one detected via DSC (1388 °C), the eutectoid temperature as well. As is discussed in Section 5.2, the phase sequence during heating does not agree with the data collected via DSC and microstructural investigations.

**Table 4.4:** Phase fractions as determined from Rietveld fits of XRD spectra. The samples received the indicated heat treatments and were water quenched. Low amounts of  $\beta_o$  phase are computational artifacts and could not be found with other characterization methods.

Alloy	Heat Treatment		Phase Fraction/%		
	$T/^\circ\text{C}$	$t/\text{h}$	$\alpha_2$ Ti <sub>3</sub> Al	$\beta_o$ Ti	$\gamma$ TiAl
Ti–42.5Al–4Zr	1200	2	58.5	2.3	39.2
	1250	2	77.7	2.9	19.4
	1320	1	98.7	1.3	0.0
Ti–44.5Al–4Zr	1200	2	52.3	6.0	41.7
	1250	2	58.7	6.5	34.8
	1320	1	71.7	2.1	26.2
Ti–46.5Al–4Zr	1200	2	71.7	2.1	26.2
	1250	2	35.8	0.7	63.5
	1360	1	33.9	3.6	62.5
Ti–48.5Al–4Zr	1200	2	9.1	6.1	84.8
	1250	2	13.6	6.7	79.7
	1320	1	61.4	2.2	36.4
Ti–49.5Al–4Zr	1200	2	2.0	4.2	93.8
	1320	1	30.1	3.9	66.0

#### 4.2.4 Nanoindentation

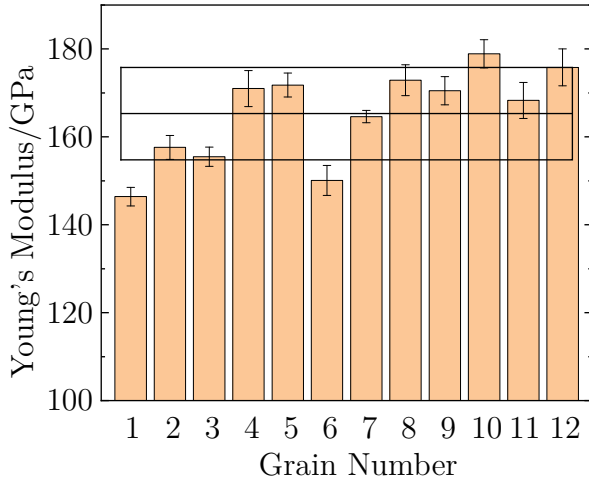
The results from nanoindentation of the  $\gamma$  phase of Ti-46.5Al-4Zr can be seen in Figure 4.7. The average Young's modulus over the twelve tested grains is  $165.3 \text{ GPa} \pm 10.5 \text{ GPa}$ , the average hardness  $4.30 \text{ GPa} \pm 0.55 \text{ GPa}$ . Using EBSD, the directional dependencies of the values for single grains were established. Figure 4.8 shows the results for both mechanical properties plotted in inverse pole figures. Each point corresponds to a specific crystallographic orientation. In both plots, only eleven points appear because grains 1 and 6 from Figure 4.7 have the same orientation. When looking at the results, no clear overall trend can be found. It seems that there is a decrease in Young's modulus and hardness going from the [111] to the [101] direction. There is a lack of data around the [001] direction that makes it harder to establish definite trends for the whole spectrum of crystal orientations. Furthermore, the directional proximity of relatively high to relatively low mechanical property values suggests that more sophisticated methods might be needed for future investigations of direction dependence.

### 4.3 Ti-Al-8Zr

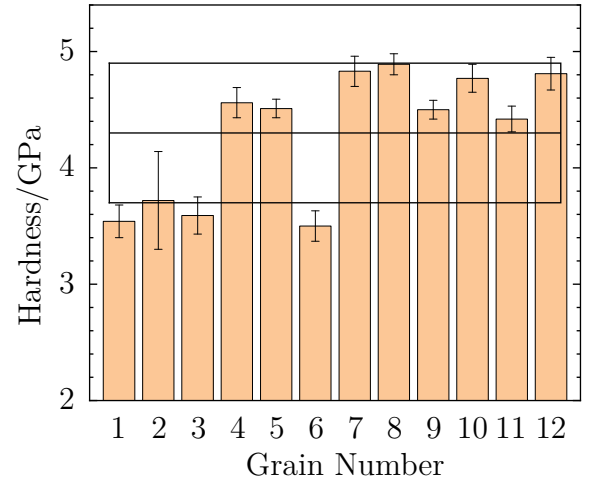
Only two phase transitions could be found in the Ti-46.8Al-8.0Zr sample by means of high-energy XRD, see Table 4.5. The eutectoid temperature at around  $1250 \text{ }^\circ\text{C}$  is significantly higher than for lower Zr contents. After going through the  $\alpha + \gamma$  two-phase field, the sample hit solidus temperature at  $1340 \text{ }^\circ\text{C}$ . The investigated spectra showed the appearance of a  $\beta$  peak close to solidus temperature. The existence of an  $\alpha + \beta + \gamma$  three-phase region, as was suggested for this alloy by Schulz [26], cannot be excluded.

**Table 4.5:** Phase transition temperatures for Ti-46.3Al-4.4Zr and Ti-46.8Al-8.0Zr as determined with synchrotron radiation.

Alloy	Transition Temperature/ $^\circ\text{C}$			
	$\alpha_2 + \gamma \rightarrow \alpha + \gamma$	$\rightarrow \alpha + \beta + \gamma$	$\rightarrow \alpha + \beta$	$\rightarrow \alpha + \beta + \text{L}$
Ti-46.3Al-4.4Zr	1155	1338	1341	1400
	$\alpha_2 + \gamma \rightarrow \alpha + \gamma$	$\rightarrow \alpha + \gamma + \text{L}$		
Ti-46.8Al-8.0Zr	1250	1340	—	—

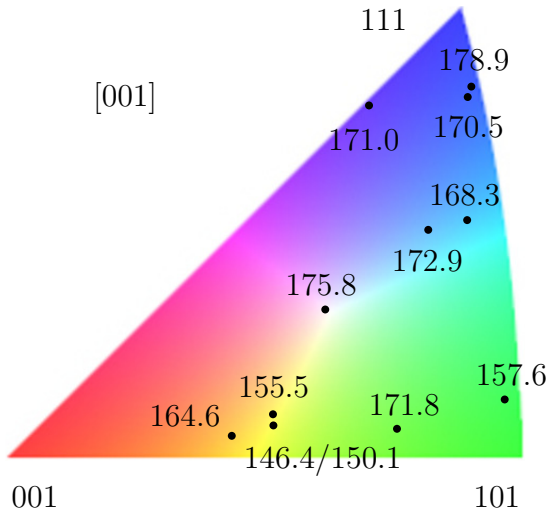


(a) Nanoindentation modulus

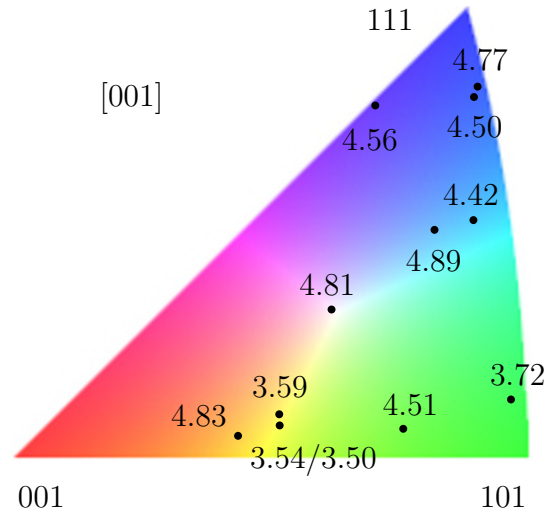


(b) Nanoindentation hardness

**Figure 4.7:** (a) Young's modulus and (b) hardness of the  $\gamma$  phase in Ti-46.5Al-4Zr as determined via nanoindentation. Several indents per grain were taken; plotted are the average values and standard deviations for each grain. The black box marks the average and standard deviation over all the grains,  $165.3 \text{ GPa} \pm 10.5 \text{ GPa}$  for Young's modulus and  $4.30 \text{ GPa} \pm 0.55 \text{ GPa}$  for hardness. The plot design was adopted from [26].



(a) Young's modulus/GPa



(b) Hardness/GPa

**Figure 4.8:** Inverse pole figures in [001] direction showing (a) Young's modulus and (b) hardness of the  $\gamma$  phase in Ti-46.5Al-4Zr as determined by nanoindentation. Grains 1 and 6 in Figure 4.7 have the same orientation, values for both grains are given here. There is an apparent increase in both Young's modulus and hardness going from [101] to [111].

## 4.4 Phase Diagrams

A section of the binary Ti–Al phase diagram according to [9] is shown in Figure 4.9(a). A goal of this work was to find the influence of Zr addition on phase transition temperature shifts in the compositional range between 42.5 at.% and 49.5 at.% Al. A corresponding high temperature section of an isopleth (constant composition section) for Ti–Al–2Zr can be seen in Figure 4.9(b). The binary phase diagram is indicated with gray lines in the background of the isopleth. The boundaries of the phase regions were determined through DSC measurements and microstructure investigations. A prominent feature of the proposed isopleth for Ti–Al–2Zr is its lowered solidus temperature compared to the binary Ti–Al phase diagram. As a consequence, the  $\alpha$  single-phase region is shrunk. While it is 130 °C high for Ti–46.5Al, the alloying of 2 at.% Zr decreases its stability range by about 50 °C to 60 °C. The maximum Al content up to which  $\beta$  Ti is present could not be determined with certainty. It appears to be lower than in the binary Ti–Al system. The  $\alpha + \gamma + L$  three-phase triangle appearing at about 49 at.% Al was included because, at 1436 °C and thus clearly above solidus temperature, there is a distinct peak in the DSC curve for Ti–49.5Al–2Zr, compare Figure 4.3(d). For all Al contents, the eutectoid

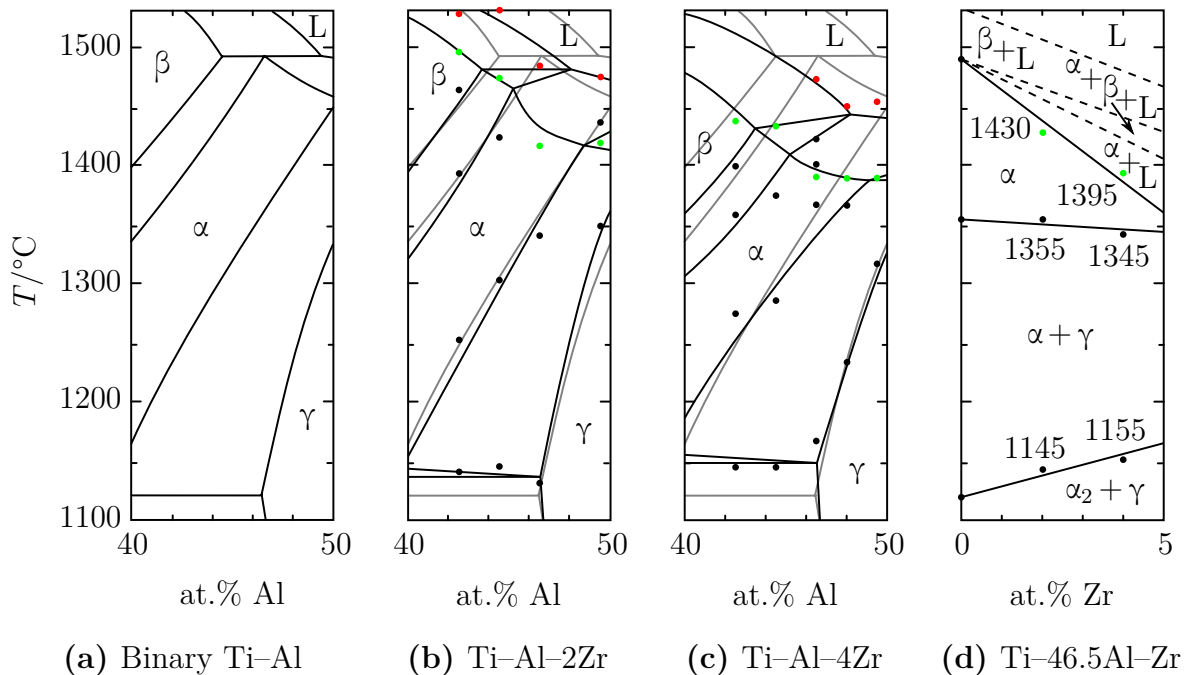


**Figure 4.9:** (a) Section of the binary Ti–Al phase diagram as given by [9], modified. (b) Isoplethal section for Ti–Al–2Zr, (c) for Ti–Al–4Zr and (d) for Ti–46.5Al–Zr. Gray lines in the background show the corresponding section from the binary Ti–Al phase diagram. Black and colored dots mark the phase transition temperatures measured in DSC. Solidus temperatures are designated with green dots, liquidus temperatures with red ones.

temperature  $\alpha_2 + \gamma \rightarrow \alpha + \gamma$  was found to be higher than in the binary system.

Figure 4.9(c) shows the proposed isopleth for Ti–Al–4Zr. Eutectoid temperature is further increased compared to the isopleth for 2 at.% Zr, solidus and liquidus temperatures are lowered. For Ti–46.5Al–4Zr, the temperature stability range of the  $\alpha$  single-phase region is narrower than for lower Zr contents, its height is about 50 °C. As is discussed in Section 5.3, the positions of the  $\beta$  and L corners of the  $\alpha + \beta + L$  three-phase triangle are not certain. They have been placed in the isopleths in a way that best fits their surroundings.

An isopleth for a constant Al content of 46.5 at.% can be seen in Figure 4.9(d). The temperatures given in the diagram are taken from the isopleths of Figure 4.9(b) and Figure 4.9(c), the values for 0 at.% Zr were taken from [9]. With increasing Zr content, the described rise in eutectoid temperature as well as the decrease of solidus temperature is visible. Above solidus temperature, the lines have been drawn in the only way that is thermodynamically possible, though their position could not be determined exactly. For this reason, they are drawn dashed and not solid.

## 4.5 Oxidation Resistance

Qualitative, macroscopic investigations of samples heat treated in atmosphere showed worse oxidation behavior for alloys high in Zr. For nanoindentation, samples were held for 23 h at 1300 °C and then furnace cooled. After this heat treatment, a weakly adhering and several mm thick oxide layer could be observed on the surface of Zr-rich alloys, see Figure 4.10. The cube of Ti–46.5Al–2Zr showed a convex surface due to oxide growth. For a Zr content of 4 at.%, cracking of the oxide scale was already present, i.e. it could easily be peeled off of the sample. During furnace cooling, the oxide scale of the alloy with 8 at.% Zr fell off on its own, without mechanical disturbance.

Sample mass was weighed before and after heat treatment. The mass increase for all samples is given in Table 4.6. As can be seen, the relative mass increase due to oxidation is higher for the alloys with high Zr content. A second iteration of this experiment showed comparable results.





**Figure 4.10:** Samples after heat treatment for 23 h at 1300 °C in atmosphere. Increasing Zr content from left to right: Ti-46.5Al, Ti-46.5Al-2Zr, Ti-46.5Al-4Zr and Ti-46.5Al-8Zr. Convex surfaces of the cubes and cracks in the oxide scale are more pronounced the higher the Zr content of the sample. Scale bar length is 2 cm.

**Table 4.6:** Sample mass of different alloys and their mass increase due to oxidation. Heat treatment (HT) was done in atmosphere for 23 h at 1300 °C with subsequent furnace cooling. Prior to HT, the samples had comparable surface areas.

Alloy	Mass Before HT/g	Mass After HT/g	Mass Increase/%
Ti-46.5Al	2.44	3.30	35.2
Ti-46.5Al-2Zr	3.29	4.55	38.3
Ti-46.5Al-4Zr	2.43	3.69	51.9
Ti-46.5Al-8Zr	4.24	6.60	55.7

# Chapter 5

## Discussion

### 5.1 Microstructural Characterization

As mentioned in Section 4.2.2, it is not known what is responsible for the needle-like structures in the micrograph of Ti–42.5Al–4Zr at 1390 °C in Figure 4.5(k). Widmanstätten  $\alpha$  plates that precipitate during cooling from the  $\beta$  single-phase field usually show a basket-weave structure. Though, according to [4], they only form at relatively low cooling rates. The samples in Figure 4.5 were water quenched, which makes the formation of Widmanstätten plates of  $\alpha$  Ti improbable. On the other hand, the cooling rates during water quenching are not high enough for a martensitic transformation of  $\beta$  to  $\alpha'$  in bulk samples. The sample of Figure 4.5(k) is thus assumed to be in the  $\alpha + \beta$  two-phase field at 1390 °C, not in the  $\beta$  single-phase field.

The inhomogeneous microstructure of Ti–42.5Al–4Zr in Figure 4.5(f) does not resemble  $\beta/\beta_0$  Ti which, as obtained from DSC data, should be the solitary phase at 1430 °C. Liquid phase would characteristically infiltrate the sample from the edges inward, surrounding single grains of the solid phase and separating them from each other. Such a pattern was not detected in the polarized light micrograph of the sample. However, during water quenching, it is possible for  $\beta$  Ti to undergo a massive phase transformation to  $\alpha$  Ti [4], which could be responsible for the non-uniform grain sizes and inhomogeneous appearance of the sample's microstructure. This would mean that the sample was in fact in the  $\beta$  single-phase field at heat treatment temperature.

A fully dendritic microstructure is visible in the micrograph for Ti–49.5Al–4Zr in Figure 4.5(e). The sample is speculated to have molten completely and to have resolidified, leading to the observed microstructure. It is not clear how the sample could retain its shape above liquidus temperature. The formation of thick oxide scales during heat treatment, as observed in Section 4.5, makes it conceivable that the melt was contained inside the scales without being able to escape. Further experiments are needed to verify this theory.

## 5.2 High-Energy X-ray Diffraction

The complementary results obtained by means of synchrotron radiation for Ti–46.5Al–2.1Zr do not agree with the experimental data of this alloy from microstructural and DSC investigations. A reason for the lower transition temperatures found during synchrotron investigations might be a detachment of the thermocouple from the sample at high temperatures. This would make temperature control faulty. Note that not just the transition temperatures for Ti–46.5Al–2Zr, but also the phase sequence during heating differs from the one found in microstructural investigations. The  $\beta$  phase could not be detected before solidus temperature in any of the other investigations performed on this alloy. To gain certainty in this respect, synchrotron measurements will have to be repeated with optimized parameters in the future.

For Ti–46.3Al–4.4Zr, synchrotron investigations yielded a phase sequence where no  $\alpha$  single-phase field is present, see Table 4.5. For Ti–46.5Al–2Zr, the  $\alpha$  single-phase region spans about 90 °C. It is therefore implausible that it should have completely disappeared at 4 at.% Zr. Furthermore, the sample in Figure 4.6 clearly showed high-temperature  $\alpha + L$  microstructure, suggesting that it passed through an  $\alpha$  single-phase region during heating. A faulty detection of  $\beta$  phase during synchrotron investigations could be responsible for the questionable phase sequence. If the  $\beta$  phase were taken from the transformations of Table 4.5, the phase sequence and transition temperatures would support the isopleth of Figure 4.9(c).

## 5.3 Phase Diagrams

The law of adjoining phase regions states that *as a phase boundary line is crossed, one and only one phase either appears or disappears* [39]. When the eutectoid line is crossed in the binary Ti–Al phase diagram, this rule holds true because, for a short time, three phases are present at the eutectoid point:  $\alpha + \gamma \rightarrow \alpha + \alpha_2 + \gamma \rightarrow \alpha_2 + \gamma$ . According to Gibbs' phase rule, at constant pressure

$$F = C - P + 1. \quad (5.1)$$

At the eutectoid point there are no available degrees of freedom ( $F = 0$ ), because in this case, three phases  $P$  coexist in a system with two components  $C$ . In ternary systems  $C = 3$ , which means that for three phases in equilibrium  $F = 3 - 3 + 1 = 1$ . For that reason, in ternary phase diagrams three phases occur in a three-phase region and not in a single line. As a consequence, the horizontal lines of binary systems open up to triangles in isopleths of ternary systems, under the condition that the section is parallel to one of the binary systems.

As deduced above, these triangular three-phase regions are thermodynamically required when transitioning from one two-phase field to another in ternary systems. For this reason, they are indicated in the isopleths of Figure 4.9 even though they could not be detected during DSC measurements. Conventional XRD was also not able to resolve the small volume fractions of  $\beta/\beta_0$  phase in the samples. The appearance of three phase fields above the solidus temperature could however be verified during synchrotron investigations. Contrary to the transition temperatures, the phase fractions obtained from synchrotron data do not help in constructing phase diagrams via tie lines. As Pelton [39] states, tie lines in ternary systems do not generally lie within the planes of isopleths and can thus not be used in determining phase boundaries there. If all tie lines lie within the plane of an isoplethal section, it is called a quasi-binary phase diagram. Only in this case, the lever rule can be applied to determine the compositions of phases in equilibrium. This is not the case for the isoplethal sections presented in this work, as can be seen for example from the tie lines for the  $\alpha + \beta$  phase region in Figure 2.4(b). The tie lines found by [6] are not parallel to the binary Ti–Al system.

For the alloy Ti–46.5Al–2Zr, the DSC curve in Figure 4.3(c) does not suggest the transformations  $\alpha + L \rightarrow \alpha + \beta + L$  and  $\alpha + \beta + L \rightarrow \beta + L$  between solidus (1416 °C) and liquidus (1484 °C). This would mean that the sample undergoes the  $\alpha + L \rightarrow L$  transformation instead. In support of this is the  $\alpha + L$  high-temperature microstructure of the sample heat treated very close to liquidus temperature, at 1470 °C, in Figure 4.2. On the other hand, it seems implausible that the L corner of the  $\alpha + \beta + L$  three-phase region be shifted to such low Al contents (< 46.5 at.%) compared to the peritectic reaction in binary Ti–Al (49.5 at.%, according to [9]). Thus, in the isopleth of Figure 4.9(b), the three-phase triangle extends a little beyond the Al content of 46.5 at.%. It could be stretched even further to the right.

The  $\alpha$  corner of the  $\alpha + \beta + L$  three-phase triangle has to be located somewhere between 44.5 at.% and 46.5 at.% Al in both isopleths of Figure 4.9. The sudden drop in solidus temperature going from one Al content to the other is thermodynamically inconceivable otherwise. The  $\beta$  corner of the three-phase region was placed to fit the DSC data best. Its exact location could not be determined.

Concerning the increase of eutectoid temperature with Zr content, Schulz [26] found the opposite trend. He assumed the eutectoid temperature for binary Ti–46.5Al to be at 1200 °C, even though he cited Schuster and Palm [9], who found 1120 °C. The eutectoid temperature for Ti–46.5Al–2Zr given in this work (about 1145 °C) is the same as the one found by Schulz [26] (1148 °C). For Ti–46.5Al–8Zr, he could not detect the eutectoid reaction  $\alpha_2 + \gamma \rightarrow \alpha + \gamma$  in DSC measurements. Rather, he estimated the temperature of a reaction  $\alpha_2 + \gamma \rightarrow \alpha + \beta + \gamma$  to be below 1050 °C. Connected with the temperature values

for the eutectoid reactions at lower Zr contents, this gives the impression of the eutectoid temperature falling with the addition of Zr. As can be seen from Figure 4.9(d), in this work, samples with added Zr had an increased eutectoid temperature compared to Ti–Al.

Kahrobaee and Palm [14] stated that alpha solvus temperature  $\alpha + \beta \rightarrow \beta$  is lowered by the addition of Zr. The isopleth in Figure 4.9(c) is in support of this statement, though for 2 at.% Zr, the effect could not be observed. The reason for this and other small deviations in the phase diagram studies of this work could be small variations in the alloying contents of the samples. Since many phase boundary lines in the binary phase diagram of Figure 4.9(a) are close to vertical, small changes in Al content lead to large changes in phase transition temperatures. Also, as was described in Section 3.1, the manufacturing of this work’s alloys resulted in Zr variations of up to 0.4 at.% for the same nominal composition. Because of this, the sample material used in this work needs to undergo chemical analysis to determine the exact alloy compositions. Appel *et al.* [4] also put forward that phase equilibria in the Ti–Al system are particularly sensitive to impurities of O. It would be interesting to see, whether the high O uptake of samples during heat treatment described in Section 4.5 leads to a compositional change of the sample below the oxide scale. If this is the case, samples would have to be heat treated under protective atmosphere to limit oxidation.

## 5.4 X-ray Diffraction

The detection of up to 6.7%  $\beta_o$  phase in the heat treatment studies of Section 4.2.3 is caused by faulty Rietveld fitting. In addition to correctly detecting and fitting the  $\alpha/\alpha_2$  and  $\gamma$  peaks, the diffraction analysis software TOPAS tried to fit a shallow but broad  $\beta_o$  peak into the diffraction spectra, leading to the observed phase fractions. This can be solved by just loading the  $\alpha$  Ti and  $\gamma$  TiAl structure files, but not the  $\beta$  Ti one. Though in this way, TOPAS will not detect small amounts of  $\beta_o$  phase in the sample in case they are in fact present.

## 5.5 Nanoindentation

Table 5.1 shows the values for nanoindentation hardness and Young’s modulus of the  $\gamma$  phase in this work compared to the ones Schulz [26] found. Though the data fit the overall trend of higher mechanical property values with increasing Zr content, the statistical significance for such an interpretation might be lacking. The average value for Young’s modulus of Ti–46.5Al–4Zr, 165.3 GPa, lies within the standard deviations of all other Young’s moduli. This does not apply to the hardness values, where the overlap of standard deviations is less pronounced.

## 5.6 Oxidation Resistance

In literature, no previous research for Ti–Al–Zr oxidation behavior at high temperatures and comparable Zr contents could be found. It is therefore not possible to put the results of Section 4.5 into perspective. Since the oxidation experiments of this work were a byproduct of sample heat treatments, the temperature of 1300 °C was not chosen specifically to investigate oxidation behavior. As Appel *et al.* [4] stated, this is far above conventional service temperatures for Ti–Al engineering alloys. Thus, although the oxidation behavior described in Section 4.5 shows a certain trend, the results cannot be applied to practical applications of these alloys. In case ternary Ti–Al–Zr alloys also show worse oxidation behavior than Ti–Al alloys under service conditions, they will have to receive some kind of oxidation protection treatment [28].

**Table 5.1:** Mechanical properties of the  $\gamma$  phase as determined in this work (Ti–46.5Al–4Zr) and by Schulz [26] (the remaining alloys). An apparent upward trend with Zr content can be noticed at least for nanoindentation hardness.

Alloy	in GPa	
	Nanoindentation Hardness	Young’s Modulus
Ti–46.5Al	$3.49 \pm 0.25$	$161.3 \pm 9.5$
Ti–46.4Al–2.1Zr	$4.22 \pm 0.46$	$170.4 \pm 8.1$
Ti–46.5Al–4Zr	$4.30 \pm 0.55$	$165.3 \pm 10.5$
Ti–46.7Al–8.0Zr	$5.03 \pm 0.54$	$177.3 \pm 12.2$

# Chapter 6

## Conclusion

In this work, the influences of 2 at.% to 4 at.% Zr on the phase transitions of Ti–Al alloys and the mechanical properties of the  $\gamma$  phase were investigated. A literature survey was done to summarize the current knowledge on Ti–Al–Zr alloys with compositions below 30 at.% Zr and around equal parts of Ti and Al. Samples with 42.5 at.%, 44.5 at.%, 46.5 at.%, 48.0 at.%, and 49.5 at.% Al were investigated for both 2 at.% and 4 at.% Zr.

The characterization methods used to get an insight into phase equilibria in the Ti–Al–Zr system were differential scanning calorimetry and *in-situ* synchrotron investigations as well as heat treatment studies and microstructural characterization using polarized light microscopy, scanning electron microscopy and electron backscatter diffraction. The mechanical properties of the  $\gamma$  phase were investigated via nanoindentation and subsequent electron backscatter diffraction was used to establish a connection between mechanical and crystallographic data. The main findings of this work are:

- With the addition of Zr, the temperature of the eutectoid transformation  $\alpha_2 + \gamma \rightarrow \alpha + \gamma$  was increased compared to the binary Ti–Al system. It was found to be 1145 °C for Ti–46.5Al–2Zr and 1155 °C for Ti–46.5Al–4Zr, compared to 1120 °C for binary Ti–46.5Al [9].
- While the  $\gamma$  solvus temperature  $\alpha + \gamma \rightarrow \alpha$  was left nearly unchanged, the addition of Zr drastically reduced the temperature stability range of the  $\alpha$  phase. This was the case because the solidus temperatures  $\alpha \rightarrow \alpha + L$  were lowered to about 1430 °C for Ti–46.5Al–2Zr and 1395 °C for Ti–46.5Al–4Zr. The  $\alpha$  single-phase region is thus reduced in height from 130 °C for binary Ti–46.5Al [9] to 50 °C with the addition of 4 at.% Zr.
- Not only solidus temperature but also liquidus temperature is lowered compared to the binary system. This effect could not be quantified reliably with the investigation methods employed in this work and will have to remain subject to further research.

- Analysis of samples with varying Al contents yielded isoplethal (constant composition) sections from 40 at.% to 50 at.% Al for both Ti–Al–2Zr and Ti–Al–4Zr.
- The oxide scales formed by alloys with increased Zr contents are more prone to cracking and generally adhere less strong to the sample surface. This could be demonstrated qualitatively during heat treatment of the samples. The mass increase for comparable heat treatments is also higher for Zr-rich samples.
- The average Young’s modulus over 12 indented  $\gamma$  grains was  $165.3 \text{ GPa} \pm 10.5 \text{ GPa}$ , the average indentation hardness  $4.30 \text{ GPa} \pm 0.55 \text{ GPa}$ . A relationship between crystallographic orientation and mechanical properties of  $\gamma$  TiAl could not be proven, though an increase in hardness and Young’s modulus going from the [101] toward the [111] direction seems likely.

In retrospect, improvements upon the experiments of this work as well as topics for further research come to mind. For one, some samples used in this work displayed an actual composition deviating from their nominal one. Detailed chemical analysis of these alloys will show whether corrective measures have to be applied to the found phase transition temperatures and isoplethal sections. Secondly, the stress state under the indenter tip during nanoindentation is multiaxial. It is therefore difficult to say whether nanoindentation results do apply to measurements of the directional dependence of mechanical properties. To find this dependence for  $\gamma$  TiAl, compression of micropillars could provide the necessary uniaxial loading conditions in further research. Lastly, knowledge on the exact location of the  $\beta$  corner of the  $\alpha + \beta + L$  three-phase region might prove useful when planning and performing heat treatments of Ti–Al–Zr alloys in the future.



# Bibliography

- [1] J. Bresler, “Influence of the alloying elements niobium, tantalum and zirconium on the high temperature properties of fully lamellar titanium aluminides,” (in German), Ph.D. dissertation, Faculty of Engineering, Friedrich-Alexander University, Erlangen-Nürnberg, Germany, 2019. DOI: 10.25593/978-3-96147-240-6.
- [2] T. Kawabata, H. Fukai, and O. Izumi, “Effect of ternary additions on mechanical properties of TiAl,” *Acta Materialia*, vol. 46, no. 6, pp. 2185–2194, 1998. DOI: 10.1016/S1359-6454(97)00422-9.
- [3] Z. Deng, D. Zhao, Y. Huang, L. Chen, H. Zou, Y. Jiang, and K. Chang, “Ab-initio and CALPHAD-type thermodynamic investigation of the Ti–Al–Zr system,” *Journal of Mining and Metallurgy, Section B: Metallurgy*, vol. 55, no. 3, pp. 427–437, 2019. DOI: 10.2298/JMMB181022039D.
- [4] F. Appel, J. Paul, and M. Oehring, *Gamma Titanium Aluminide Alloys*. Weinheim, Germany: Wiley-VCH, 2011. DOI: 10.1002/9783527636204.
- [5] F. Yang, F. Xiao, S. Liu, S. Dong, L. Huang, Q. Chen, G. Cai, H. Liu, and Z. Jin, “Isothermal section of Al–Ti–Zr ternary system at 1273 K,” *Journal of Alloys and Compounds*, vol. 585, pp. 325–330, 2014. DOI: 10.1016/j.jallcom.2013.09.082.
- [6] R. Kainuma, Y. Fujita, H. Mitsui, I. Ohnuma, and K. Ishida, “Phase equilibria among  $\alpha$  (hcp),  $\beta$  (bcc) and  $\gamma$  ( $L1_0$ ) phases in Ti–Al base ternary alloys,” *Intermetallics*, vol. 8, no. 8, pp. 855–867, 2000. DOI: 10.1016/S0966-9795(00)00015-7.
- [7] A. Grytsiv, P. Rogl, H. Schmidt, and G. Giester, “Constitution of the ternary system Al–Ru–Ti (aluminum-ruthenium-titanium),” *Journal of Phase Equilibria*, vol. 24, no. 6, pp. 511–527, 2003. DOI: 10.1361/105497103772084552.
- [8] V. Witusiewicz, A. Bondar, U. Hecht, S. Rex, and T. Velikanova, “The Al–B–Nb–Ti system: III. Thermodynamic re-evaluation of the constituent binary system Al–Ti,” *Journal of Alloys and Compounds*, vol. 465, no. 1–2, pp. 64–77, 2008. DOI: 10.1016/j.jallcom.2007.10.061.

- [9] J. Schuster and M. Palm, “Reassessment of the binary aluminum-titanium phase diagram,” *Journal of Phase Equilibria and Diffusion*, vol. 27, no. 3, pp. 255–277, 2006. DOI: 10.1361/154770306X109809.
- [10] Y. Kim, “Microstructural evolution and mechanical properties of a forged gamma titanium aluminide alloy,” *Acta Metallurgica et Materialia*, vol. 40, no. 6, pp. 1121–1134, 1992. DOI: 10.1016/0956-7151(92)90411-7.
- [11] H. Doi, K. Hashimoto, K. Kasahara, and T. Tsujimoto, “Site determination of third elements in TiAl compound by X-ray diffractometry,” *Materials Transactions, JIM*, vol. 31, no. 11, pp. 975–982, 1990. DOI: 10.2320/matertrans1989.31.975.
- [12] D. Abreu, A. Silva, J. Santos, D. Barros, C. Barros, N. Chaia, C. Nunes, and G. Coelho, “Liquidus projection of the Al–Ti–Zr system,” *Journal of Alloys and Compounds*, vol. 849, no. 156463, pp. 1–9, 2020. DOI: 10.1016/j.jallcom.2020.156463.
- [13] H. Clemens and S. Mayer, “Design, processing, microstructure, properties, and applications of advanced intermetallic TiAl alloys,” *Advanced Engineering Materials*, vol. 15, no. 4, pp. 191–215, 2013. DOI: 10.1002/adem.201200231.
- [14] Z. Kahrobaee and M. Palm, “Critical assessment of the Al–Ti–Zr system,” *Journal of Phase Equilibria and Diffusion*, vol. 41, pp. 687–701, 2020. DOI: 10.1007/s11669-020-00837-x.
- [15] M. Turchanin, P. Agraval, and A. Abdulov, “Thermodynamic assessment of the Cu–Ti–Zr system. II. Cu–Zr and Ti–Zr systems,” *Powder Metallurgy and Metal Ceramics*, vol. 47, no. 7–8, pp. 428–446, 2008. DOI: 10.1007/s11106-008-9039-x.
- [16] E. Fischer and C. Colinet, “An updated thermodynamic modeling of the Al–Zr system,” *Journal of Phase Equilibria and Diffusion*, vol. 36, pp. 404–413, 2015. DOI: 10.1007/s11669-015-0398-y.
- [17] J. Wang, W. Zheng, G. Xu, X. Zeng, and Y. Cui, “Thermodynamic assessment of the Ti–Al–Zr system and atomic mobility of its bcc phase,” *Calphad*, vol. 70, no. 101801, 2020. DOI: 10.1016/j.calphad.2020.101801.
- [18] K. Hashimoto, H. Doi, K. Kasahara, T. Tsujimoto, and T. Suzuki, “Effects of third elements on the structures of TiAl-based alloys,” (in Japanese), *Journal of the Japan Institute of Metals*, vol. 52, no. 8, pp. 816–825, 1988. DOI: 10.2320/jinstmet1952.52.8\_816.
- [19] J. Zollinger, J. Lapin, D. Daloz, and H. Combeau, “Influence of oxygen on solidification behaviour of cast TiAl-based alloys,” *Intermetallics*, vol. 15, no. 10, pp. 1343–1350, 2007. DOI: 10.1016/j.intermet.2007.04.002.

- [20] K. Lü, F. Yang, Z. Xie, H. Liu, G. Cai, and Z. Jin, “Isothermal section of Al–Ti–Zr ternary system at 1073 K,” *Transactions of Nonferrous Metals Society of China*, vol. 26, no. 11, pp. 3052–3058, 2016. DOI: 10.1016/S1003-6326(16)64436-9.
- [21] D. Sornadurai, V. Sastry, V. Thomas Paul, R. Flemming, F. Jose, and R. Ramaseshan, “Microstructure, crystal structure and mechanical properties of the new ternary intermetallic alloy phase  $Zr_2TiAl$ ,” *Intermetallics*, vol. 24, pp. 89–94, 2012. DOI: 10.1016/j.intermet.2012.01.027.
- [22] D. Sornadurai, B. Panigrahi, V. Sastry, and Ramani, “Crystal structure and X-ray powder diffraction pattern of  $Ti_2ZrAl$ ,” *Powder Diffraction*, vol. 15, no. 3, pp. 189–190, 2000. DOI: 10.1017/S0885715600011052.
- [23] D. Tanda, T. Tanabe, R. Tamura, and S. Takeuchi, “Synthesis of ternary  $L1_0$  compounds of Ti–Al–Zr system and their mechanical properties,” *Materials Science and Engineering A*, vol. 387–389, pp. 991–995, 2004. DOI: 10.1016/j.msea.2004.01.113.
- [24] C. Rossouw, C. Forwood, M. Gibson, and P. Miller, “Zone-axis convergent-beam electron diffraction and ALCHEMI analysis of Ti–Al alloys with ternary additions,” *Philosophical Magazine A*, vol. 74, no. 1, pp. 77–102, 1996. DOI: 10.1080/01418619608239691.
- [25] Y. Hao, D. Xu, Y. Cui, R. Yang, and D. Li, “The site occupancies of alloying elements in TiAl and  $Ti_3Al$  alloys,” *Acta Materialia*, vol. 47, no. 4, pp. 1129–1139, 1999. DOI: 10.1016/S1359-6454(99)00006-3.
- [26] B. Schulz, “The effect of zirconium on titanium aluminides,” Master’s thesis, Chair of Physical Metallurgy and Metallic Materials, Montanuniversität, Leoben, Austria, 2019.
- [27] C. Zambaldi, “Micromechanical modeling of  $\gamma$ -TiAl based alloys,” Ph.D. dissertation, Faculty of Georesources and Materials Engineering, RWTH Aachen University, Aachen, Germany, 2010. DOI: rx4.
- [28] R. Pflumm, S. Friedle, and M. Schütze, “Oxidation protection of  $\gamma$ -TiAl-based alloys – a review,” *Intermetallics*, vol. 56, pp. 1–14, 2015. DOI: 10.1016/j.intermet.2014.08.002.
- [29] A. Rahmel, W. Quadackers, and M. Schütze, “Fundamentals of TiAl oxidation – a critical review,” *Materials and Corrosion*, vol. 46, no. 5, pp. 271–285, 1995. DOI: 10.1002/maco.19950460503.

- [30] M. Hasegawa, “Chapter 3.3 – Ellingham diagram,” in *Treatise on Process Metallurgy*, S. Seetharaman, Ed. Amsterdam: Elsevier, 2014, vol. 1, pp. 507–516. DOI: 10.1016/B978-0-08-096986-2.00032-1.
- [31] S. Taniguchi, H. Juso, and T. Shibata, “Improvement in high-temperature oxidation resistance of TiAl by addition of 0.2 mass% Zr,” *Materials Transactions*, vol. 37, no. 3, pp. 245–251, 1996. DOI: 10.2320/matertrans1989.37.245.
- [32] S. Woo and D. Lee, “Characterization of oxide scales formed on TiAl–W–Zr alloys,” (in Korean), *Korean Journal of Materials Research*, vol. 14, no. 6, pp. 394–398, 2004. DOI: 10.3740/MRSK.2004.14.6.394.
- [33] Y. Shida and H. Anada, “The effect of various ternary additives on the oxidation behavior of TiAl in high-temperature air,” *Oxidation of Metals*, vol. 45, no. 1–2, pp. 197–219, 1996. DOI: 10.1007/BF01046826.
- [34] V. Güther, M. Allen, J. Klose, and H. Clemens, “Metallurgical processing of titanium aluminides on industrial scale,” *Intermetallics*, vol. 103, pp. 12–22, 2018. DOI: 10.1016/j.intermet.2018.09.006.
- [35] C. Fleißner-Rieger, T. Pogrietz, D. Obersteiner, T. Pfeifer, H. Clemens, and S. Mayer, “An additively manufactured titanium alloy in the focus of metallography,” *Practical Metallography*, vol. 58, no. 1, pp. 4–31, 2021. DOI: 10.1515/pm-2020-0001.
- [36] A. Hammersley, “FIT2D: A multi-purpose data reduction, analysis and visualization program,” *Journal of Applied Crystallography*, vol. 49, pp. 646–652, 2016. DOI: 10.1107/S1600576716000455.
- [37] L. Lutterotti, “Total pattern fitting for the combined size-strain-stress-texture determination in thin film diffraction,” *Nuclear Instruments and Methods in Physics Research B*, vol. 268, no. 3–4, pp. 334–340, 2010. DOI: 10.1016/j.nimb.2009.09.053.
- [38] J. Hay, P. Agee, and E. Herbert, “Continuous stiffness measurement during instrumented indentation testing,” *Experimental Techniques*, vol. 34, no. 3, pp. 86–94, 2010. DOI: 10.1111/j.1747-1567.2010.00618.x.
- [39] A. Pelton, *Phase Diagrams and Thermodynamic Modeling of Solutions*. Amsterdam: Elsevier, 2019. DOI: 10.1016/C2013-0-19504-9.